

Polarization of seven MBM clouds at high galactic latitude

Neha, S.^{1,2*}, Maheswar, G.^{1,3}, Soam, A.⁴, Chang Won Lee^{4,5}

¹*Aryabhata Research Institute of Observational Sciences (ARIES), Nainital (Uttarakhad) – 263002, India.*

²*Pt. Ravishankar Shukla University, Raipur (Chhattisgarh) – 492010, India.*

³*Indian Institute of Astrophysics, Block II, Koramangala, Bangalore, 560 034, India*

⁴*Korea Astronomy & Space Science Institute (KASI), 776 Daedeokdae-ro, Yuseong-gu, Daejeon, Republic of Korea.*

⁵*University of Science Technology, 217 Gajungro, Yuseong-gu, 305-333 Daejeon, Republic of Korea.*

Accepted 2018, February 16. Received 2018, February 15; in original form 2018, January 04

ABSTRACT

We made R-band polarization measurements of 234 stars towards the direction of MBM 33-39 cloud complex. The distance of MBM 33-39 complex was determined as 120 ± 10 pc using polarization results and near-infrared photometry from the 2MASS survey. The magnetic field geometry of the individual cloud inferred from our polarimetric results reveals that the field lines are in general consistent with the global magnetic field geometry of the region obtained from the previous studies. This implies that the clouds in the complex are permeated by the interstellar magnetic field. Multi-wavelength polarization measurements of a few stars projected on the complex suggest that the size of the dust grains in these clouds is similar to those found in the normal interstellar medium of the Milky Way. We studied a possible formation scenario of MBM 33-39 complex by combining the polarization results from our study and from the literature and by identifying the distribution of ionized, atomic and molecular (dust) components of material in the region.

Key words: ISM: clouds; polarization: dust; ISM: magnetic fields; ISM: individual objects: MBM 33-39

1 INTRODUCTION

How cold, molecular and dense structures, that are sites of star formation, are formed from hot, atomic and diffuse gas in the interstellar medium is still unclear. Stellar feedback processes like the expansion of HII regions (Bania & Lyon, 1980; Vazquez-Semadeni et al., 1995; Passot et al., 1995) and supernova blast waves (McCray & Kafatos, 1987; Gazol-Patiño & Passot, 1999; de Avillez, 2000; de Avillez & Breitschwerdt, 2005; Ntormousi et al., 2011) are considered to be the plausible mechanisms by which hot, over pressurized bubbles are created. As these shells expand, they sweep up the surrounding medium and inject it into high galactic latitudes. The gas then tends to slide down back guided by the magnetic field lines creating large-scale flows and gather in location where infalling streams converge and shock leading to the formation of high-latitude molecular clouds (Hennebelle & Pérault, 2000; Inoue et al., 2007; Inoue & Inutsuka, 2008; Shin et al., 2008; Heitsch et al., 2009; Inoue & Inutsuka, 2012; Hennebelle, 2013; Inoue & Inutsuka, 2016). The high-latitude clouds (HLCs) generally do not have any internal energy source, but most HLCs may be affected by the mean interstellar far-ultraviolet (FUV) radiations (van Dishoeck & Black, 1988). The relatively lower densities and proximity to the Sun make the HLCs ideal objects to study the penetration of FUV

radiations, which may have an important role in the formation and evolution of these clouds and the role of the magnetic field could also be crucial in the formation process. Most of the HLCs are not gravitationally bound and hence, they do not show any signature of star formation, but a few HLCs, e.g., MBM 12 (Luhman, 2001) and MBM 20 (L1642; Malinen et al., 2014) show evidence of star formation. Thus, the star-formation is not considered to be a dominant process in most HLCs (Magnani et al., 1996).

Dutra & Bica (2002), from a heterogeneous set of surveys based on infrared, CO and optical detection methods (Magnani et al., 1985; Keto & Myers, 1986; Desert et al., 1988; Magnani et al., 1996; Reach et al., 1998), have compiled a total of 439 HLCs ($b \geq 30^\circ$). Molecular clouds are classified based on their visual extinction (A_V) along the line of sight through the clouds (van Dishoeck & Black, 1988). Clouds with $A_V < 1$ magnitude are termed as diffuse clouds and those with $A_V > 5$ magnitudes are called the dark clouds. The third category of clouds, termed as translucent clouds, are those having values of A_V lying in the range from 1 – 5 magnitudes. Out of 439, 393 clouds are found to have central A_V values less than 1 magnitude and are therefore classified as diffuse clouds. The remaining 45 clouds are classified as translucent clouds. LDN 1457 (MBM 12) is the only HLC, which was classified with $A_V > 5$ (McGehee, 2008). However, Dobashi (2011) estimated A_V values

* Email: pathakneha.sharma@gmail.com; neha.astro18@gmail.com

Table 1. Parameters of high-Galactic latitude clouds studied in this work.

S. No.	Cloud Identification	l (°)	b (°)	Opacity [†] Class	Distance [‡] (pc)	Other Designations
1.	MBM 33	359.06	36.75	4/5	89^{+18}_{-21}	LDN 1778A, LDN 1778B, LDN 1780
2.	MBM 34	2.36	35.67	-	110^{+27}_{-34}	
3.	MBM 35	6.56	38.13	-	89^{+17}_{-25}	
4.	MBM 36	4.18	35.75	5	105^{+7}_{-7}	LDN 134, LDN 134A
5.	MBM 37	5.70	36.62	5	121^{+10}_{-16}	LDN 183, LDN 184
6.	MBM 38	8.22	36.62	-	77^{+24}_{-24}	CB 68
7.	MBM 39	11.39	36.22	-	94^{+15}_{-11}	

[†] Opacity classes have been taken from [Dutra & Bica \(2002\)](#).

[‡] Distances are taken from [Schlafly et al. \(2014\)](#).

for dust clouds using Two Micron All Sky Survey Point-Source Catalog (2MASS PSC; [Cutri et al., 2003](#); [Skrutskie et al., 2006](#)) and found $A_V > 5$ for three MBM clouds, e.g., 5.44 ± 0.15 for MBM 20, 8.56 ± 0.15 for MBM 36 and 6.76 ± 0.16 for MBM 37. Thus, HLCs are predominately diffuse or translucent types. The above classification scheme also reflects the kind of astrochemistry taking place in these clouds ([van Dishoeck & Black, 1988](#)). While the chemistry in diffuse clouds is mostly due to photo-processes, dark clouds are influenced by collisional processes. Thus, it may be argued that the translucent clouds represent an intermediate stage between the diffuse and the dark clouds making them the ideal sources to study the initial stages of cloud formation.

Many authors studied the dynamical condensation process of the ISM in shocks ([Koyama & Inutsuka, 2000](#); [Inutsuka & Koyama, 2002](#); [Inutsuka et al., 2005](#)) and in converging flows ([Hennebelle & Péroult, 1999](#); [Audit & Hennebelle, 2005](#); [Heitsch et al., 2005](#); [Hennebelle & Audit, 2007](#); [Vázquez-Semadeni et al., 2006](#)). Based on magnetohydrodynamics simulations, it was shown that molecular clouds can be created behind a shock wave if it is moving roughly parallel to the mean magnetic field lines ([Inoue et al., 2007](#); [Inoue & Inutsuka, 2008, 2012, 2016](#)). A perpendicular magnetic field will decrease the compression of the post-shock gas and thus suppresses the process necessary for the rapid flow fragmentations and build-up of high density regions ([Hennebelle & Péroult, 2000](#); [Burkert & Hartmann, 2004](#); [Inoue et al., 2007](#); [Heitsch et al., 2008a,b](#)).

In this paper, we present results of our multi-wavelength (V , R , I) polarimetric observations of an HLC complex, MBM 33-39. The parameters of the seven clouds, studied in this work, are listed in Table 1. The distance of the clouds which ranges from 77 pc to 121 pc ([Franco, 1989](#); [Cernis & Straizys, 1992](#); [Magnani et al., 1996](#); [Lallement et al., 2003](#); [Schlafly et al., 2014](#)) shows that these are local clouds lying at a galactic height ranging from ~ 45 pc to ~ 70 pc. The local scale height of the molecular gas layer is estimated to be ~ 70 pc with an uncertainty of 25% ([Blitz, 1991](#)). Therefore, this complex could be considered as an example of a group located just at the boundary of the molecular gas layer in the solar vicinity. The main objectives of our study are to map the magnetic field geometry of the individual clouds in the complex and understand the relationships between the field geometry and their density structures. In this paper, section 2 explains the observations and the procedures of data reduction. Our results and discussion are described in section 3. At last, we finalize our paper by summarizing the results in section 5.

2 OBSERVATIONS AND DATA REDUCTION

Polarimetric observations were performed using the Aries IMaging POLarimeter (AIMPOL, [Rautela et al., 2004](#)). This polarimeter is

Table 2. Log of observations in the R_{kc} filter ($\lambda_{R_{kc}} = 0.760 \mu\text{m}$).

Cloud Name	Date of observations (year, month, date)
MBM 33	2015, February, 21; 2015, March 18;
	2015, April, 22
	2015, May, 14, 18, 21, 22, 24
MBM 34	2013, April, 19
	2013, May, 3, 4, 13, 14, 15, 16
MBM 35	2016, April, 6
MBM 36	2016, May, 5
MBM 38	2016, May, 10
MBM 39	2016, May, 11

used as back-end instrument at Cassegrain focus of the 104-cm Sampurnanand telescope, which is located at Aryabhata Research Institute of Observational Sciences (ARIES), Nainital, India. It is coupled with TK 1024×1024 *pixel*² CCD camera and a half-wave plate (HWP) modulator and a Wollaston prism beam-splitter are used in between. The Wollaston prism splits the light rays into two images; conventionally known as ordinary and extraordinary. The observations were made in $\lambda_{R_{kc}} = 0.760 \mu\text{m}$ photometric band. We also observed a few bright stars towards MBM 33, MBM 34 and MBM 35 in multi-wavelengths (V , R & I). The plate scale of CCD is 1.48 arcsec/pixel and field of view is ~ 8 arcmin in diameter. The full width at half maximum (FWHM) varies from 2 to 3 pixels. The Read out noise and gain of CCD are $7.0 e^{-1}$ and $11.98 e^{-1}/\text{ADU}$, respectively. Table 2 represents the details of the observations.

We executed standard aperture photometry using the Image Reduction & Analysis Facility (IRAF) software to extract the fluxes of ordinary (I_o) and extraordinary (I_e) images for all the observed stars with a good signal-to-noise ratio. The ratio $R(\alpha)$ is given by

$$R(\alpha) = \frac{\frac{I_e(\alpha)}{I_o(\alpha)} - 1}{\frac{I_e(\alpha)}{I_o(\alpha)} + 1} = P \cos(2\theta - 4\alpha) \quad (1)$$

where P is the degree of polarization; θ is the polarization position angle and α is the position of the fast axis of HWP at 0° , 22.5° , 45° and 67.5° corresponding to four normalized Stokes parameters, $q[\text{R}(0^\circ)]$, $u[\text{R}(22.5^\circ)]$, $q_1[\text{R}(45^\circ)]$ and $u_1[\text{R}(67.5^\circ)]$, respectively. We estimate the uncertainties in normalized Stokes parameters ($\sigma_R(\alpha)$) (σ_q , σ_u , σ_{q_1} , σ_{u_1}) in percent using the following equation ([Ramaprakash et al., 1998](#)),

$$\sigma_R(\alpha) = \frac{\sqrt{N_e + N_o + 2N_b}}{N_e + N_o} \quad (2)$$

where N_o and N_e are the counts of ordinary and extraordinary images, respectively, and $N_b [= (N_{be} + N_{bo})/2]$ is the mean background counts around the extraordinary and ordinary images.

[Rautela et al. \(2004\)](#); [Medhi et al. \(2008\)](#); [Eswaraiah et al.](#)

Table 3. Polarized standard stars observed in R_{kC} band.

Date of Obs.	$P \pm \epsilon_P$ (%)	$\theta \pm \epsilon_\theta$ ($^\circ$)
HD 19820		
(† Standard values: $4.526 \pm 0.025\%$, $114.46 \pm 0.16^\circ$)		
21 Feb 2015	4.4 ± 0.1	113 ± 2
HD 25443		
(† Standard values: $4.734 \pm 0.045\%$, $133.65 \pm 0.28^\circ$)		
21 Feb 2015	4.7 ± 0.1	134 ± 2
HD 154445		
(† Standard values: $3.683 \pm 0.072\%$, $88.92 \pm 0.56^\circ$)		
18 Mar 2015	3.5 ± 0.1	89 ± 2
22 Apr 2015	3.5 ± 0.2	90 ± 1
14 May 2015	3.4 ± 0.2	89 ± 1
18 May 2015	3.4 ± 0.2	89 ± 1
21 May 2015	3.4 ± 0.2	90 ± 1
22 May 2015	3.8 ± 0.2	88 ± 2
24 May 2015	3.5 ± 0.2	87 ± 2
06 Apr 2016	3.7 ± 0.1	89 ± 1
05 May 2016	3.5 ± 0.1	89 ± 1
10 May 2016	3.4 ± 0.1	88 ± 1
HD 155197		
(† Standard values: $4.274 \pm 0.027\%$, $102.88 \pm 0.18^\circ$)		
18 Mar 2015	4.2 ± 0.1	103 ± 2
22 Apr 2015	4.0 ± 0.3	103 ± 1
14 May 2015	4.1 ± 0.1	103 ± 1
18 May 2015	4.1 ± 0.1	102 ± 1
21 May 2015	4.1 ± 0.1	103 ± 1
22 May 2015	4.3 ± 0.1	103 ± 1
24 May 2015	4.1 ± 0.1	102 ± 1
06 Apr 2016	4.0 ± 0.1	102 ± 1
05 May 2016	3.7 ± 0.1	103 ± 1
10 May 2016	4.3 ± 0.1	103 ± 1
11 May 2016	4.0 ± 0.1	102 ± 1

‡ Values in R band from Schmidt et al. (1992)

(2011) observed un-polarized standard stars regularly and found that the instrumental polarization of AIMPOL on the 104-cm Sampurnanand Telescope is approximately invariable. The instrumental polarization is found to be less than $\sim 0.1\%$. To determine the reference direction of the polarizer, we have observed two polarized standard stars HD 154445 and HD 155197, adopted from Schmidt et al. (1992), on each observing night. Additionally, another two standard stars HD 19820 and HD 25443 were also observed in one night. The standard stars observed by us to calibrate our observations are reported in Table 3.

3 RESULTS

Polarization measurements of 234 stars were obtained towards the direction of seven MBM clouds. The average values of polarization measurements are presented in Table 4 (the detailed results are shown in Table 7). The columns 1 and 2 give the cloud name and the number of stars observed towards individual clouds, respectively. In columns 3 and 4 we give the mean values and the standard deviations of P and θ_P , respectively. In Figure 1, we present the $P\%$ vs. θ_P in the upper panel and the histogram of the θ_P in the lower panel. A Gaussian fit to the histogram is also shown. The mean value and the standard deviation for the 234 stars are $1.6 \pm 0.8\%$ and $83 \pm 12^\circ$, respectively.

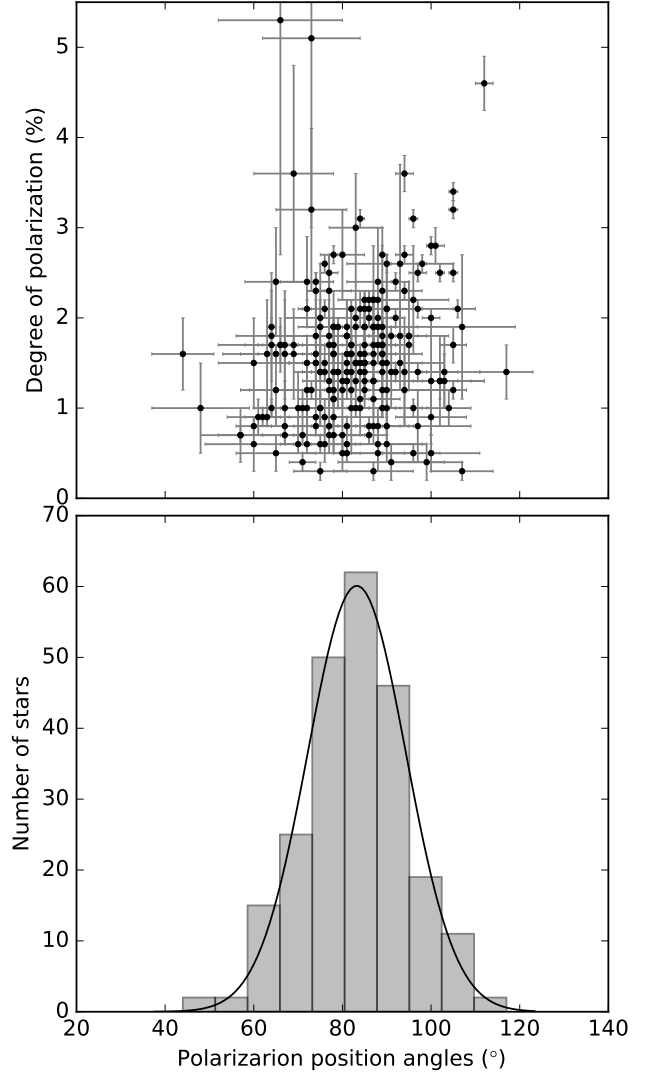


Figure 1. The degree of polarization vs. the polarization position angle of 234 stars observed towards MBM 33-39 is shown in the upper panel. The histogram of the θ_P along with a Gaussian fit is shown in the lower panel.

Table 4. Average values of polarization measurements.

Cloud Name	Number of stars observed	$\langle P \rangle$ (%)	$\langle \theta_P \rangle$ ($^\circ$)
MBM 33	49	1.3 ± 0.6	79 ± 15
MBM 34	59	1.6 ± 0.4	83 ± 9
MBM 35	21	1.5 ± 0.3	84 ± 7
MBM 36	20	2.1 ± 0.5	77 ± 9
MBM 37	26	2.6 ± 0.6	94 ± 8
MBM 38	33	1.1 ± 0.4	87 ± 11
MBM 39	26	0.8 ± 0.5	78 ± 13

Note: Column 1 represents the name of the molecular cloud; column 2 shows the total number of stars observed towards the individual cloud; column 3 denotes the mean values and standard deviations of the degree of polarization, and column 4 denotes the mean values and standard deviations of the polarization position angle.

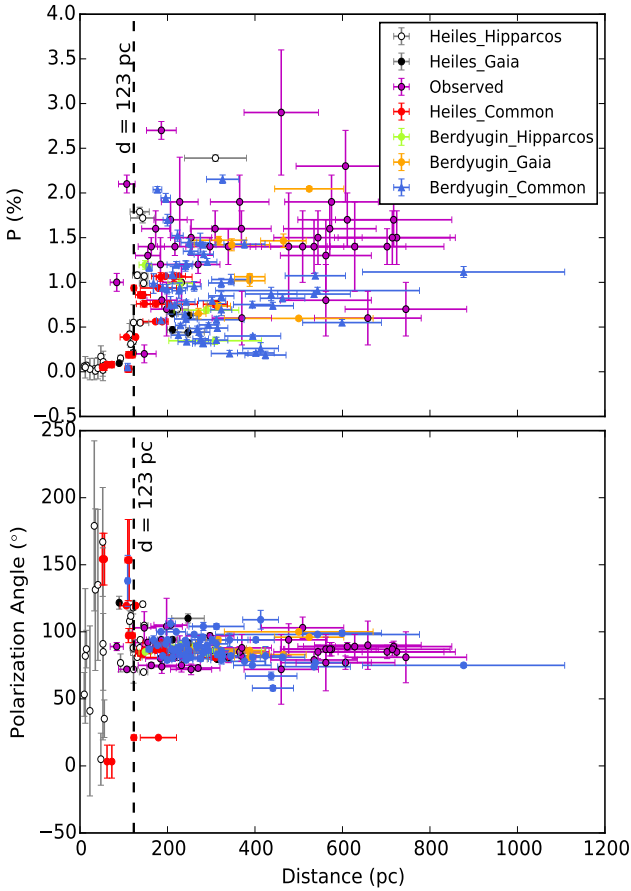


Figure 2. The degree of polarization (upper panel) and polarization position angle (lower panel) vs. distance of stars for which both polarization and distance measurements are available in the literature. The polarization and the parallax measurements are obtained from Heiles (2000); Berdyugin et al. (2000) and van Leeuwen (2007); Gaia Collaboration (2016), respectively. For the Heiles_common and Berdyugin_common stars, which have parallax measurements available in both the catalogs, we have taken the parallax values from Gaia.

4 DISCUSSION

4.1 Distance of the complex

4.1.1 From polarization measurements

The distance estimated using parallax measurements and the polarization measurements of stars projected onto the clouds could be considered as more reliable because of the fact that both the measurements are independent of the properties of the observed stars. In addition to this, the measured polarization position angles provide an additional clue to the presence of the most dominant dust layer along a given line of sight. While the foreground stars would show relatively large dispersion in the values of polarization position angles, the stars that lie behind the cloud layer, inferred from the high degree of polarization values, would show less dispersion with a constant value depending upon the plane of the sky orientation of the local magnetic field.

We searched for stars with polarization measurements available in the catalogs by Heiles (2000) and Berdyugin et al. (2000) within a region of $20^\circ \times 20^\circ$ around MBM 33-39 complex. We obtained 51 stars for which polarization measurements are available in Heiles (2000) and 76 stars from Berdyugin et al. (2000). We obtained

parallax measurements for these stars from van Leeuwen (2007) and Gaia Collaboration (2016). For 40 Heiles sources we obtained parallax measurements from van Leeuwen (2007) and for 19 Heiles stars, we obtained parallax measurements from Gaia Collaboration (2016). Of these, 12 stars were common in both. Similarly, 67 sources from Berdyugin et al. (2000) have parallax measurements in van Leeuwen (2007), 72 stars have parallax measurements in Gaia Collaboration (2016). Of these, 63 stars were common in both. Only those stars are selected for which the ratio of the parallax and the error in the parallax is greater than or equal to 2. In Figure 2 we show the degree of polarization (above) and polarization position angle (below) vs. distance estimated from the van Leeuwen (2007) using open circles for Heiles stars and from the Gaia Collaboration (2016) using filled circles in black for Heiles stars. The green-yellow circles represent the Berdyugin stars having distance from van Leeuwen (2007) and orange circles correspond to Berdyugin stars that have distance from Gaia Collaboration (2016). The Heiles stars that are common in both van Leeuwen (2007) and Gaia Collaboration (2016) are identified using red, while the Berdyugin common stars are shown using blue color. The magenta circles represent the observed sources for which the distances have been determined using the procedure described in section 4.1.2.

A significant increase in the values of the degree of polarization is found to occur at ~ 120 pc (marked using dashed line). The dispersion in the values of the polarization position angle was also found to be relatively large for sources lying till ~ 120 pc. Beyond this distance, the mean value of the polarization position angle is found to be 88° , which is very much similar to the mean value of the sources observed by us towards the MBM 33-39 cloud complex. Based on the 2MASS photometry (Cutri et al., 2003), using the $J - H$ and $H - K_s$ colors (described briefly in section 4.1.2), we estimated the distance and A_V of stars for which we have polarization observations. We selected sources having photometric errors in $JHK_s \leq 0.035$. Of the 234 stars observed by us, we could estimate distance and A_V values for 41 of them which follow all our selection criteria. Majority of the sources are lying beyond the ~ 120 pc distance of the complex. The mean value of the polarization position angle of these 41 sources is found to be 85° implying that the magnetic field of the MBM 33-39 cloud complex is similar to those present in the ambient interstellar medium.

4.1.2 From the 2MASS photometry

Using the near-IR photometric method (Maheswar et al., 2010), we estimated the distance to the MBM 33-39 cloud complex. A short description of the method¹ is described here. The method uses an approach in which the stars lying in the regions containing the clouds are classified into main sequence and giants using near-IR colors. The observed $(J - H)$ and $(H - K_s)$ colors of the stars having $(J - K_s) \leq 0.75$ are de-reddened using trial values of A_V simultaneously and plotted in $(J - H)$ vs. $(H - K_s)$ color-color (CC) diagram. The JHK_s values are from the 2MASS catalog (Cutri et al., 2003). We have considered only those sources for which the photometric errors in JHK_s are ≤ 0.035 and also are lying within the cloud boundary inferred from the $160 \mu\text{m}$ images of the clouds obtained by AKARI satellite. In Fig. 3, we identified sources selected based on the above criteria towards MBM 33 on the $160 \mu\text{m}$ image of the cloud. A normal interstellar extinction law

¹ For a more attentive analysis on the uncertainties and limitations of the method, refer Maheswar et al. (2010)

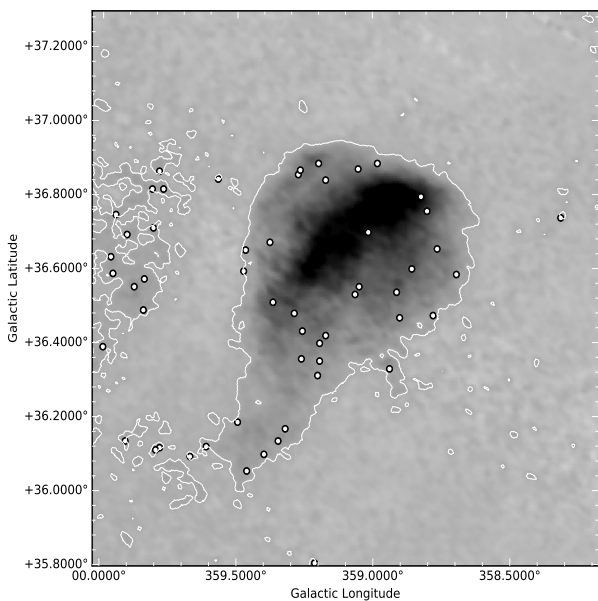


Figure 3. AKARI L-band ($160\ \mu\text{m}$) image of MBM 33 cloud. The open circles show the stars lying inside the outermost contour of the image.

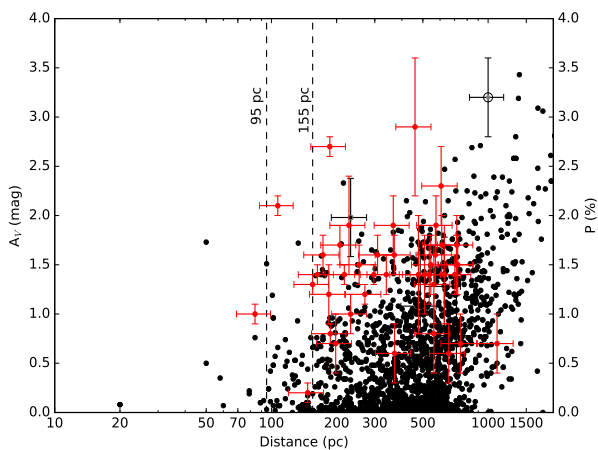


Figure 4. A_V vs. distance plot for the stars (black circles) belong to the regions containing HLCs, MBM 33-39 complex. The dashed vertical lines are drawn at 95 pc and 155 pc inferred from the method described in Maheswar et al. (2010). Typical error bars are shown on a few data points. The degree of polarization ($P\%$) is also plotted along second Y-axis using red circles.

(Rieke & Lebofsky, 1985) is used for the de-reddening procedure. The spectral type corresponding to the minimum value of the χ^2 produced by the best fit of the de-reddened colors to the intrinsic colors is assigned to the star. Thus, the stars, which are classified as main sequence stars, are plotted in an A_V versus distance diagram to estimate the distance of the cloud. This method was used to estimate distances to a number of clouds (e.g., Maheswar et al., 2011; Soam et al., 2013; Eswaraiyah et al., 2013; Neha et al., 2016).

In Fig. 4, we show the A_V versus distance diagram for the sources selected towards all the seven MBM clouds using filled circles in black. The 41 sources for which we made polarization measurements and estimated their distance and A_V using the 2MASS photometry are also plotted using filled circles in red. A significant increase (~ 1 magnitude) in the values of A_V is apparent at ~ 95 pc.

A second increase in the A_V (~ 2 magnitude) is occurring at ~ 155 pc. The distance of the majority of the sources observed by us are also found to be lying beyond 155 pc and show higher values of A_V (~ 2 magnitude).

Distance to interstellar material present in a region covering an area of $8^\circ \times 9^\circ$ towards MBM 33-39 complex was obtained by Franco (1989) using four color $uvby$ and $H\beta$ photometry of 81 stars which are of A and F spectral types. Franco (1989) assigned a distance of 110 ± 10 pc to all the interstellar material lying towards the region of study. Schlafly et al. (2014) presented a catalog of distances to molecular clouds in which they estimated distances to the majority of the clouds identified by Magnani et al. (1985). Schlafly et al. (2014) estimated distances to the molecular clouds using optical photometry of stars obtained from PanSTARRS-1. They used the technique of Green et al. (2014) to obtain distance and reddening of individual stars. The distances obtained by Schlafly et al. (2014) are presented in Table 1. According to Schlafly et al. (2014), the clouds in MBM 33-39 complex is lying in the range of ~ 80 – 120 pc within the uncertainty of ~ 10 – 30% .

The change in the values of the polarization position angles from being random to a more regular value of about 88° is seen clearly in Fig. 2 for stars with distance $\gtrsim 120$ pc. It is at this distance and beyond that, the values of the degree of polarization are also becoming significantly high. The results obtained from polarization measurements indicate that the high density material towards the MBM 33-39 complex is most likely lying at a distance of ~ 120 pc with an uncertainty of 10%.

4.2 Magnetic field morphology of the region

This work presents the first polarimetric results of a high galactic latitude cloud complex that contains both translucent as well as the dark molecular cloud (Toth et al., 1995; Kirk et al., 2009). The initial study of interstellar polarization towards high galactic regions of north and south Galactic poles was made by, for example, Appenzeller (1968); Mathewson & Ford (1970); Markkanen (1979); Korhonen & Reiz (1986); Berdyugin et al. (2000); Berdyugin & Teerikorpi (2001); Berdyugin et al. (2001, 2004); Berdyugin et al. (2014, 2011) made polarization measurements of high galactic latitude ($30^\circ < b < 70^\circ$) field stars that are lying in the longitude range of $240^\circ < l < 360^\circ$, $0^\circ < l < 60^\circ$ and $240^\circ < l < 360^\circ$. The main aim of their study was to make a comprehensive polarization map of the region and understand the patterns, and its relation to the local dust and gas shells and with the local spiral arm. The most remarkable feature seen in their study is a loop like structure centered at $l \approx 330^\circ$ which was noticed in previous studies also (Ellis & Axon, 1978; Mathewson & Ford, 1970). It was suggested that the local super bubble or the Loop I (Large et al., 1966; Berkhuijsen et al., 1971) is responsible for the observed polarization pattern seen in their study. The MBM 33-39 complex considered in this study is lying in the longitude range of $359^\circ < l < 360^\circ$, $0^\circ < l < 12^\circ$ and latitude range of $35^\circ < b < 39^\circ$. The magnetic field geometry of the MBM 33-39 complex traced in this study will be useful to understand the relationship between the large scale and individual cloud scale magnetic field orientation and their relationship with the material structures of the cloud.

Fig. 5 shows the polarization vectors of MBM 33, 34, 35, 36, 37, 38 and 39 superposed on their corresponding AKARI Infrared Astronomy Satellite $160\ \mu\text{m}$ images. The $160\ \mu\text{m}$ image shows the intensity of the cold dust emission from the clouds. In Fig. 5 (a) we present the polarization vectors of 49 stars observed towards MBM 33. The cloud shows a cometary shape with the head oriented

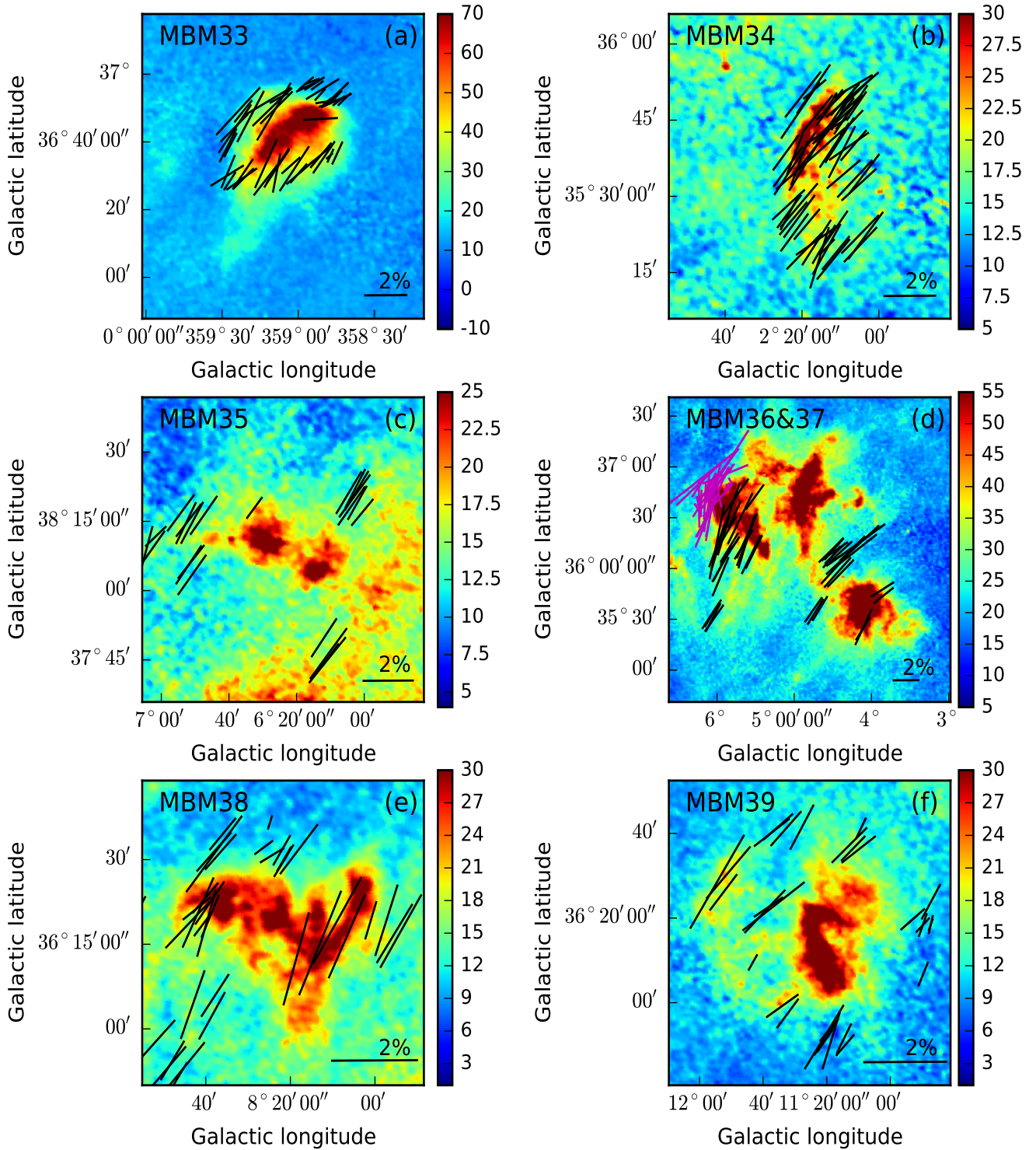


Figure 5. Polarization vectors (depicting the magnetic field morphology) in black color drawn on the AKARI $160\ \mu\text{m}$ images of seven MBM clouds are shown in (a), (b), (c), (d), (e), (f), respectively. The NIR polarization vectors for MBM 37, taken from Clemens (2012), are also plotted in magenta color.

away from the Galactic plane. The high density part of the cloud is oriented along the north-west and south-east direction of the main body of the cloud. The magnetic field lines inferred from the polarization vectors are also oriented parallel to this high density structure of the cloud. Among the seven clouds studied here, MBM

33 shows the largest value of dispersion in polarization position angles (15°).

In Fig. 5 (b) we show the polarization vectors for MBM 34, which lies about 3° east of MBM 33. The $160\ \mu\text{m}$ emission shows a curved cloud structure as we move from the north towards east. Towards the north-eastern edge, the polarization vectors seem to

follow the curvature of the cloud though, in general, the magnetic field is oriented parallel to the global field direction. The polarization vectors towards MBM 35 is shown in the Fig. 5 (c). The cloud shows two relatively dense condensations. A line joining these two structures is oriented almost perpendicular to the mean direction of the magnetic field lines. The two condensations could have been formed as a result of fragmentation of the cloud essentially occurred perpendicular to the direction of the mean magnetic field. The emission from the low density material in the south-western parts of the two condensations is distributed almost parallel to the magnetic field orientation.

In Fig. 5 (d) we show the polarization vectors for MBM 36 and MBM 37. MBM 36 is also identified as LDN 134 (Lynds, 1962). It shows a spherical shape. Projected magnetic field inferred from the optical polarization measurements shows a smooth distribution. The magnetic field is well aligned with the global magnetic field mapped by Berdyugin et al. (2011, 2014). MBM 37 (= LDN 134N, LDN 183) harbors a starless centrally condensed (~ 180 visual magnitude), high column density prestellar core. This core has been studied extensively in different spectroscopic species (Dickens et al., 2000; Lee et al., 2001; Pagani et al., 2005, 2007) and in far-infrared and sub-millimeter continuum (Juvela et al., 2002; Ward-Thompson et al., 2002; Lehtinen et al., 2003; Pagani et al., 2003; Kirk et al., 2005; Kauffmann et al., 2008). This core is considered to be much more evolved than many other prestellar cores (Dickens et al., 2000) and also shows ample evidence of it being in the verge of initiating star formation (Lee et al., 2001). Three spatially and kinematically distinct sub-cores have been identified towards the densest part of LDN 183 (Kirk et al., 2009). Based on the results obtained, Kirk et al. (2009) proposed that LDN 183 is a prestellar core which is currently fragmenting, collapsing and rotating about its inner magnetic field inferred from sub-mm observations. The core is spinning up as it collapses and may form a multiple protostellar systems.

In Fig. 6 we show a close-up view of LDN 183 region. The black vectors represent the polarization measurements made by us. The near-infrared polarization vectors measured by Clemens (2012) are plotted in white. Crutcher et al. (2004) made SCUBA² polarization measurements around LDN 183 and observed 25 independent positions. The mean value of all the sub-mm polarization position angles corrected for the 90° rotation to infer the projected magnetic field orientation in the inner high-density region of LDN 183 is shown using a red line. The rotation axis identified by Kirk et al. (2009) is shown using an orange line. The outer projected magnetic field inferred from the optical polarization measurements is well aligned with the field orientation of the loop structure. The long axis of the cloud is found to be roughly perpendicular to the outer magnetic field projected on the sky plane suggesting that the accumulation of the material occurred along the magnetic field lines. Based on ^{12}CO emission, Goldsmith et al. (2008) showed the striation patterns that are aligned with the local magnetic field which suggests a strong coupling between the magnetic field and the ISM. In LDN 183 also we see such patterns in the low density regions (Fig. 6) that are found to be aligned with the local magnetic field inferred from our polarization vectors. These striations are either due to the Kelvin-Helmholtz instability or magnetosonic waves propagating through the envelope of the cloud (Heyer et al., 2016). The high

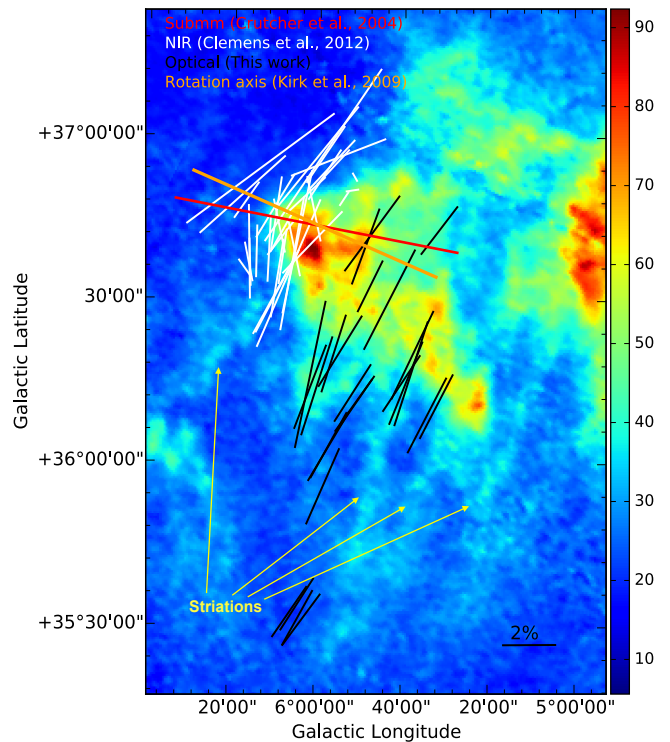


Figure 6. AKARI $160\ \mu\text{m}$ images of MBM 37. The observed optical polarization vectors are plotted in black color, NIR polarization vectors, taken from Clemens (2012), are plotted in white color. The red vector shows the magnetic field orientation inferred from the averaged sub-mm polarization vector corrected for 90° (Crutcher, 2004). The orange vector represents the cloud’s rotation axis Kirk et al. (2009).

density part of the cloud where near-infrared polarization measurements are made by Clemens (2012), the vectors follow the curvature of the cloud. It is interesting to note that the curved part of LDN 183, MBM 38 and MBM 39 together they form part of a peculiar structure identified using a dotted line in Fig. 7. The rotation axis of LDN 183 (Kirk et al., 2009) is oriented parallel to the inner magnetic field but lying perpendicular to the outer magnetic field (all the quantities are in the sky plane). The projected field lines inferred from sub-mm and optical/near-infrared are found to be oriented perpendicular to each other. This has also been noticed in our previous study towards IRAM04191+1522 (Soam et al., 2015). Further, the polarization vectors obtained from optical observations are almost perpendicular to the long axis of LDN 183 while the polarization vector obtained from submillimeter observations is roughly parallel to the long axis of L183. Since, the former likely traces the densest part of LDN 183 while the later likely traces the diffuse part of LDN 183, this may mean that the inner region of LDN 183 is close to the supercritical status while the outer region of L183 is in subcritical status.

The polarization vectors towards MBM 38 and MBM 39 are shown in the Fig. 5 (e, f). MBM 38 lies on the periphery of the structure identified with a broken line in red on Fig. 7. The plane of the sky magnetic field lines in both MBM 38 and 39 are found to be distributed smoothly. In MBM 38, the long axis of the cloud is found to be roughly perpendicular to the magnetic field lines. In MBM 39, similar to MBM 33 and 34, the material structure shows a curved orientation which is not apparent in the magnetic field map

² SCUBA camera is mounted on JCMT, which is operated by the Joint Astronomy Center, Hawaii, on behalf of the UK PPARC, the Netherlands NWO, and the Canadian NRC.

owing to a few number of stars observed which are projected over the structure.

Planck Collaboration et al. (2016) studied the MBM 33-39 cloud complex and mapped sub-mm magnetic field morphology around this region (see Fig. 18 in Planck Collaboration et al., 2016). They found that the magnetic field geometry is aligned with the matter at high Galactic latitudes in diffuse ISM. Our optical magnetic field map is found to be consistent with the Planck sub-mm magnetic field map, where polarization is caused by the emission from dust grains. The large-scale magnetic field structure shown in Fig. 8 is also found to be consistent with all-sky Planck sub-mm magnetic field map (see Fig. 5 in Planck Collaboration et al., 2015).

4.3 Magnetic field strength

We estimated the plane-of-the-sky component of magnetic field strength (B_{pos}) in HLCs using the updated Chandrasekhar-Fermi (CF) relation (Chandrasekhar & Fermi, 1953; Ostriker et al., 2001; Crutcher, 2005):

$$B_{pos} = 9.3 \sqrt{n(\text{H}_2)} \frac{\Delta V}{\delta \theta} \quad (3)$$

In this equation, $n(\text{H}_2)$ represents the number density of the molecular hydrogen in molecules cm^{-3} , ΔV is the full-width half maximum of CO line in km s^{-1} and $\delta \theta$ shows the dispersion in polarization position angle θ_P in degrees. Chandrasekhar & Fermi (1953) assumed an equipartition between the kinetic and perturbed magnetic energies and it was suggested that the plane-of-the-sky component of magnetic field strength could be estimated using together with the velocity dispersion and polarization position angle dispersion. For molecular clouds, MBM 33, MBM 36, MBM 37, MBM 38 and MBM 39, we obtained the number density and the CO line width (ΔV) values from Laureijs et al. (1995) and for MBM 34, we used the mean value of all the number densities and the ΔV value is taken from Hartmann et al. (1998). The values of $\delta \theta$ for all the clouds are estimated from the standard deviation in polarization angle θ_P . The $\delta \theta$ values are corrected for the uncertainties in polarization angle θ_P (Lai et al., 2001; Franco et al., 2010). Using these values in equation 3, we estimated the value of B_{pos} . The values of number density, $\delta \theta$, ΔV and magnetic field strength for the six clouds are listed in Table 5. The strength of the magnetic field range from ~ 10 – $40 \mu\text{G}$. The strongest field strength is found in LDN 183 (MBM 37) and the weakest field is found in MBM 33.

4.4 Possible influence of local environment and magnetic field in the formation of MBM 33-39 complex

In order to examine the kind of environment prevails in the close vicinity of MBM 33-39 complex, we made a color composite image of the region containing the MBM 33-39 cloud complex. In Fig. 8 we show the color composite image of $70^\circ \times 70^\circ$ region centered at $l = 335^\circ$ and $b = +20^\circ$. It is created using $\text{H}\alpha$ image (red), 857 GHz Planck image (green) and atomic hydrogen column density map (blue) all obtained from the SkyView³. The red color shows the distribution of the ionized gas in this region. The ionized region is primarily distributed around the ζ Ophiuchus (Sh2-27, Sharpless,

1959) and the Sco OB2 (Sh2-7, Sharpless, 1959) association which are identified and labeled. Some of the members of the Scorpius-Centaurus association (LCC = Lower Centaurus-Crux, UCL = Upper Centaurus-Lupus, and US = Upper Scorpius) obtained from Bobylev & Bajkova (2007) are identified using black-yellow circles. Distribution of O-type stars towards displayed region obtained from Maíz-Apellániz et al. (2004) is also shown using filled black circles. The location of the MBM 33-39 cloud complex is identified using a rectangular box. The polarization vectors measured by Berdyugin et al. (2014) are also over-plotted for better visualization.

Clearly, there are a number of loop structures visible in the Fig. 8. A small-scale loop structure of ionized gas is noticeable towards the northern part of the Sh2-7 which is followed by another bigger loop of HI gas, Loop I (Large et al., 1966). There is one more loop which is identified with Hercules ridge (Fejes & Wesselius, 1973). Both the bigger loops are conspicuous in the 857 GHz Planck image which traces the distribution of cold interstellar dust grains and in the polarization map produced by Berdyugin et al. (2014). According to the basic concept of star formation history of the Scorpius-Centaurus association (de Geus, 1992; Toth et al., 1995; Preibisch & Zinnecker, 1999), the star formation process started in the UCL association some 15 Myr ago. The most massive member of UCL exploded as a supernova about 12 Myr ago, which formed most of the HI shells in the vicinity of the association. As the shock wave produced by this supernova passed through US some 5 Myr, it triggered star formation there. Stellar winds from the massive members of US initiated to spread the molecular cloud and paused the star formation process. About 1.5 Myr ago, the most massive member in the US went off as a supernova which fully dispersed the parent molecular cloud. The passage of the shock wave about 1 Myr ago has triggered recent star formation in ρ Oph. Thus there has been at least two events of supernova explosions in the vicinity of the location where MBM 33-39 cloud complex is situated. A link between the Loop I and the runaway star ζ Ophiuchus was suggested by Berkhuijsen et al. (1971). The distance of ζ Ophiuchus corresponding to a parallax of 8.91 (0.2) mas (van Leeuwen, 2007) is $\sim 110 \pm 3$ pc. Thus ζ Ophiuchus is about 35 pc from the MBM 33-39 complex and hence MBM 33-39 cloud complex might be currently interacting with the stellar wind and the ionizing radiation from ζ Ophiuchus also. These interactions probably might have driven the large-scale flows of material, guided by the large-scale magnetic field, that is required for the initiation of cloud formation. The alignment between the matter structure in the ISM and the magnetic field shows evidence of the formation of cold neutral filaments through turbulence. The condensation of cold gas out of warm neutral medium could be triggered by the local environment (Audit & Hennebelle, 2005; Inoue & Inutsuka, 2009; Heitsch et al., 2009; Saury et al., 2014). Scenario in which if the gas velocity is dynamically aligned with the magnetic field, the gas condensations tend to get stretched due to turbulent shear creating filaments and sheets, which would emerge elongated in column density maps. On the other hand, if the velocity shear stretches the matter into filaments, due to flux freezing, the field also gets stretched creating alignments between the magnetic field and the cold condensations (Hennebelle, 2013). In MBM 33 and 34, the structures seem to be aligned with the projected magnetic field. In MBM 35, though the high density structure is aligned perpendicular to the projected magnetic field, the diffused emission seems to be parallel to the field.

Based on a quantity which is a normalized velocity difference of peak velocities of optically thick and thin lines, Lee & Myers (2011) have classified MBM 37 (LDN 183) as a contracting

³ SkyView has been developed with generous support from the NASA AISR and ADP programs (P.I. Thomas A. McGlynn) under the auspices of the High Energy Astrophysics Science Archive Research Center (HEASARC) at the NASA/ GSFC Astrophysics Science Division.

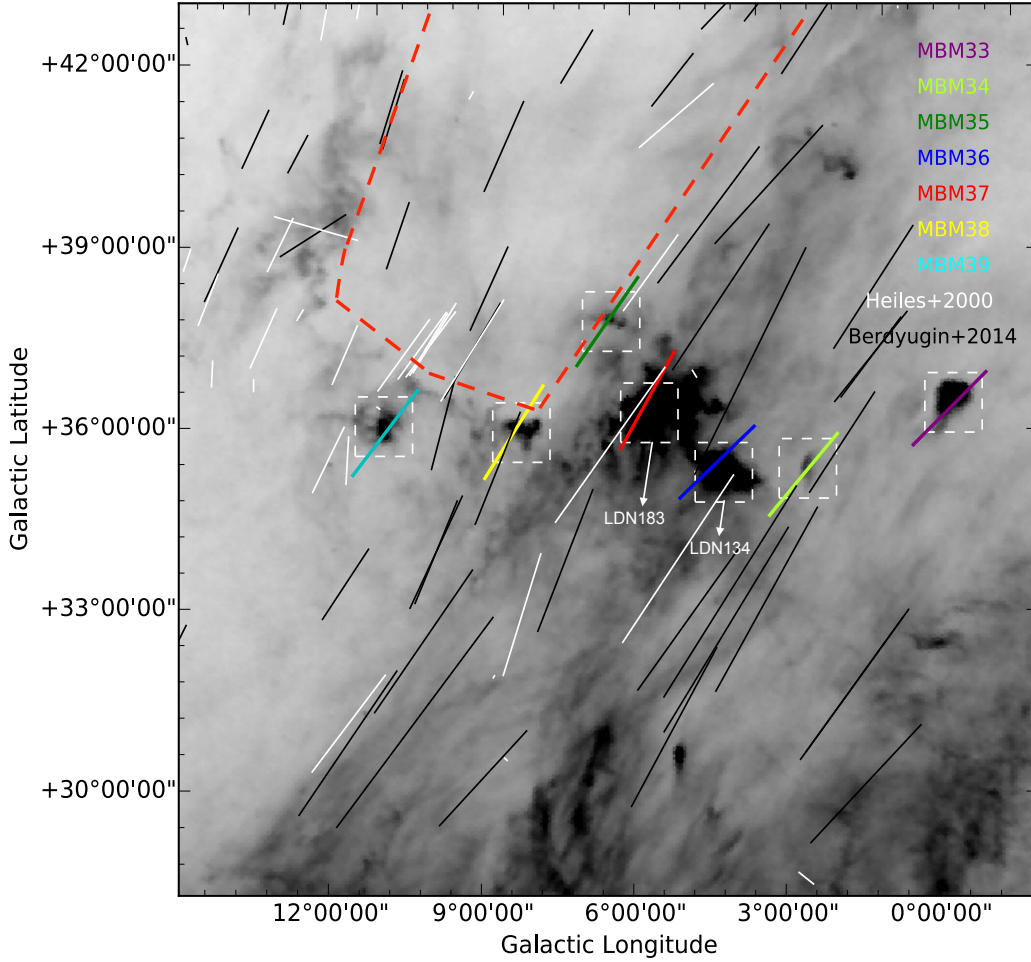


Figure 7. $15^\circ \times 15^\circ$ Planck 857 GHz image of MBM 33-39 cloud complex. The observed mean polarization vectors corresponding to each cloud are overlotted. The white and black polarization vectors, taken from Heiles (2000) and Berdyugin et al. (2000), respectively, are also overlotted. White boxes identify each cloud. A peculiar U-shape structure is shown by dashed-line in red.

Table 5. The magnetic field strength in HLCs.

Cloud Name	Number Density (cm^{-3})	$\delta\theta$ ($^\circ$)	ΔV (km s^{-1})	B (μG)	Reference
MBM33	990	15	0.55	11	a
MBM34	966	9	0.70	22	b
MBM36	905	9	1.04	32	a
MBM37	878	8	1.23	42	a
MBM38	835	12	0.54	12	a
MBM39	1220	13	0.58	14	a

a - Laureijs et al. (1995)

b - Hartmann et al. (1998)

core. When a gravitationally bound structure forms, an equipartition between gravitational and turbulent energies are expected and turbulence becomes super-Alfvénic (sub-Alfvénic) for supercritical (sub-critical) structures. For sub-critical structures, the magnetic field is dynamically important and draws matter preferentially parallel to the field lines. This results in the formation of sheet-like structures which subsequently get fragmented to form elongated filaments. The presence of striations perpendicular to the high-column density ridge of MBM 37 supports this picture of cloud formation. Such striations perpendicular to the high-column density filaments have been noticed in the Herschel maps of nearby molecular clouds,

like Taurus (Palmeirim et al., 2013). The magnetic field strength estimated for the MBM 33-39 clouds are typical of low to moderate strength. Though the projected envelop magnetic field inferred from the optical polarization is consistent with the standard model of cloud collapse, almost orthogonal orientation of the projected magnetic field at the inner regions of MBM 37 inferred through sub-mm polarization (Crutcher et al., 2004) is puzzling. The rotation axis of the cores identified by Kirk et al. (2009) is also found to be aligned with this inner magnetic field. Magnetic field orientation of more fainter stars need to be made to obtain a much clear picture

of the role played by the magnetic field in the formation of first translucent and then dark high density clouds in ISM.

4.5 Serkowski's law

The value of P strongly depends on the wavelength, which is known as the polarization curve, described by the Serkowski law (Serkowski et al., 1975) as follows:

$$P_{\lambda} = P_{max} \exp\left[-K \ln^2\left(\frac{\lambda_{max}}{\lambda}\right)\right]. \quad (4)$$

Here, P_{λ} is the degree of polarization in percentage at wavelength λ and P_{max} is the maximum degree of polarization in percentage at wavelength λ_{max} . The parameter K which was originally taken to be fixed at a value of $K = 1.15$, which determines the width of the peak in the curve. We studied the dust properties of MBM clouds using the Serkowski's relation (equation 4). The equation 4 provides the relation between the maximum degree of polarization P_{max} and corresponding wavelength λ_{max} for each star. We calculated the P_{max} and λ_{max} using the weighted least-squares fitting to the measured polarization in V, R and I bands to equation 4 by assuming $K = 1.15$. The origin of the polarization can also be inferred by the λ_{max} values. The stars having much lower λ_{max} values than the mean value of the interstellar medium ($0.55 \mu\text{m}$; Serkowski et al., 1975) may possess an intrinsic component of polarization. Fig. 9 shows the Serkowski fitting for 27 stars towards MBM 33, MBM 34 and MBM 35. We also plotted their Serkowski fitting curve in the same figure. In the figure, two stars having star IDs 1 and 6, have one of the data points lying outside the best-fitted curve within errors. Moreover, for stars with star IDs 1 and 22, the ratio of the degree of polarization and polarization uncertainty (P_V/ϵ_{P_V}) is less than 3. Therefore, we have excluded these three stars. The weighted average values of the P_{max} and λ_{max} with weighted standard deviations for remaining 27 stars are found to be $1.5 \pm 0.4 \%$ and $0.54 \pm 0.08 \mu\text{m}$, respectively.

The estimated λ_{max} is quite similar to the value corresponding to the general interstellar medium ($0.55 \mu\text{m}$; Serkowski et al., 1975) within error limits. We estimated the value of R_V , the total-to-selective extinction, using the relation $R_V = (5.6 \pm 0.3) \times \lambda_{max}$ (Whittet & van Breda, 1978), for all the stars. The R_V values range from 1.95 to 3.80 for all the stars. The weighted average value of R_V for 27 stars is found to be 2.9 ± 0.5 , which is consistent with the mean value ($R_V = 3.08$) for the Milky Way Galaxy, suggesting that the dust grain size within the MBM 33, MBM 34 and MBM 35 clouds is normal. The error in R_V has been estimated by error propagation in the above equation. Table 6 shows the fitting parameters P_{max} , λ_{max} and R_V values for all the stars.

5 CONCLUSION

We made polarimetric observations of 234 stars that are located towards the direction of a high galactic latitude cloud complex, MBM 33-39. The complex contains clouds that are of both translucent and dark molecular cloud types. Thus, the study of this complex provides us a unique opportunity to understand the role played by the magnetic field in the early stages of cloud formation mechanism. A summary of the important results obtained from this study is listed below:

1. By combining our polarization results and those from the literature, we estimated distance to the complex. The distances of

the individual stars are determined using the parallax measurements made by Hipparcos and/or GAIA. We estimated a distance of $\sim 120 \pm 10$ pc for the complex. The advantage of using polarization results and parallax measurements is that the distance determination is independent of the properties of the observed stars.

2. The magnetic field geometry of the individual clouds inferred from our polarimetric results reveals that the field lines are in general consistent with the global magnetic field geometry of the region obtained from the previous studies. This implies that the clouds in the complex are permeated by the interstellar magnetic field.

3. The dust structures of the individual clouds inferred from $160 \mu\text{m}$ images from AKARI are found to be either parallel or perpendicular to the magnetic field suggesting that magnetic field played an important role in the formation process of these structures in the cloud.

4. The dispersion of polarization angles is found to be maximum in the MBM 33 suggesting that the cloud is in a state of dynamical evolution possibly due to its interaction with external triggers.

5. In MBM 37 (=LDN 183), the most evolved cloud in the complex, the magnetic field direction inferred from our optical polarization measurement which traces field lines of the periphery of the cloud is found to be oriented almost orthogonal to the field directions of the denser inner regions of the cloud traced by the sub-mm polarization measurements.

6. Multi-wavelength polarization measurements of a few stars projected on the clouds suggest that the dust grain size in these clouds is similar to those found in the normal interstellar medium of the Milky Way.

7. A possible formation scenario of MBM 33-39 complex is discussed by combining the polarization results from our study (and from the literature) and by identifying the distribution of ionized, atomic and molecular (dust) components of material in the region.

ACKNOWLEDGEMENTS

The authors thank anonymous referee for the helpful and constructive comments. This research has made use of the SIMBAD database, operated at CDS, Strasbourg, France. We also acknowledge the use of NASA's *SkyView* facility (<http://skyview.gsfc.nasa.gov>) located at NASA Goddard Space Flight Center. This publication makes use of data products from the Two Micron All Sky Survey (2MASS), which is a joint project of the University of Massachusetts and the Infrared Processing and Analysis Center/California Institute of Technology, funded by the National Aeronautics and Space Administration and the National Science Foundation. CWL was supported by Basic Science Research Program through the National Research Foundation of Korea (NRF) funded by the Ministry of Education, Science. NS acknowledge Dr. A. K. Pandey (ARIES, Nainital, India) for his support. NS thanks Suvendu Rakshit (SNU, Seoul, Republic of Korea) for carefully reading the manuscript.

REFERENCES

- Appenzeller I., 1968, *ApJ*, **151**, 907
 Audit E., Hennebelle P., 2005, *A&A*, **433**, 1
 Bania T. M., Lyon J. G., 1980, *ApJ*, **239**, 173
 Berdyugin A., Teerikorpi P., 2001, *A&A*, **368**, 635
 Berdyugin A., Teerikorpi P., Haikala L., 2000, *A&A*, **358**, 717

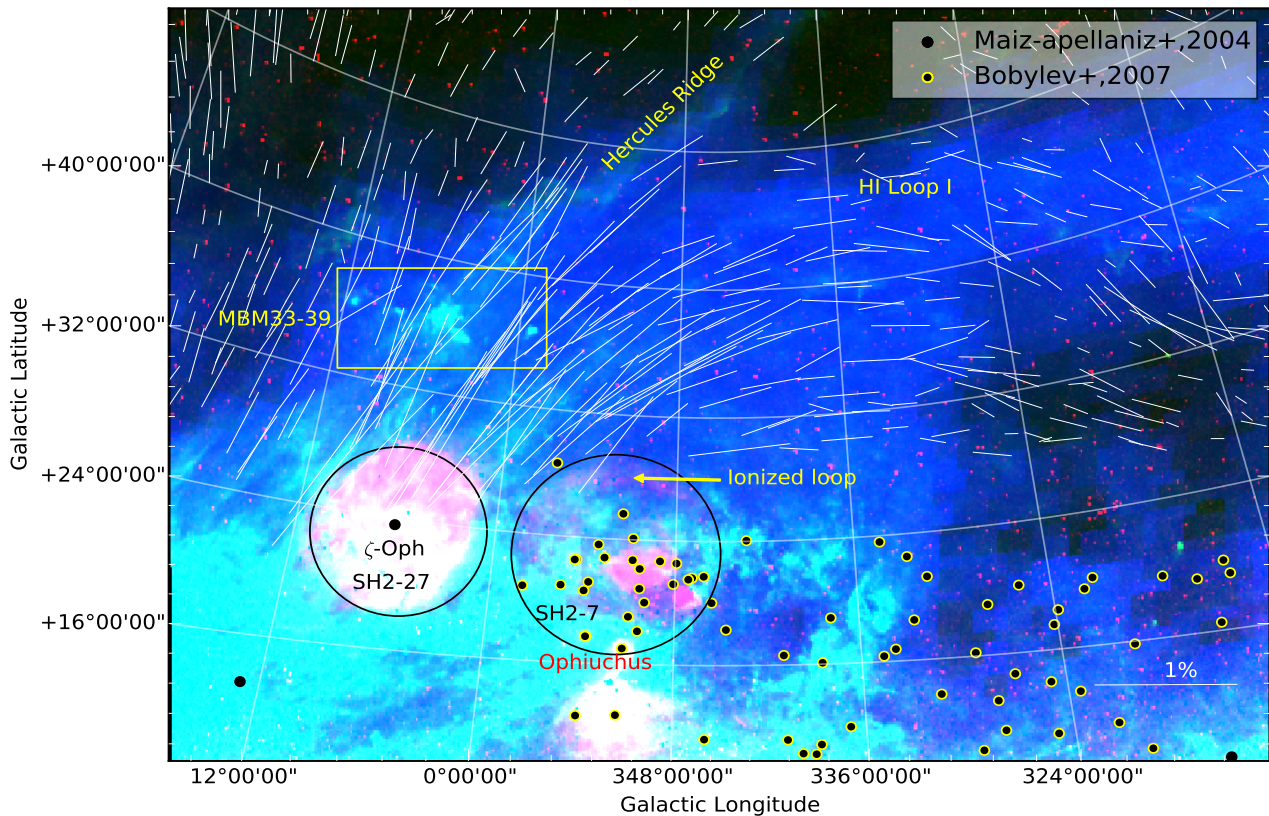


Figure 8. The $70^\circ \times 70^\circ$ color composite image of the Sco-Cen region which contain MBM 33-39 cloud complex centered at $l = 345^\circ$ and $b = +25^\circ$. The red, green and blue colors correspond to $H\alpha$ image, 857 GHz Planck image and nH image obtained from the SkyView. The polarization vectors in white, taken from Berdyugin et al. (2000), are also overlotted. A vector with 1% polarization is shown as scale.

Berdyugin A., Teerikorpi P., Haikala L., Hanski M., Knude J., Markkanen T., 2001, *A&A*, **372**, 276
 Berdyugin A., Piirola V., Teerikorpi P., 2004, *A&A*, **424**, 873
 Berdyugin A., Piirola V., Teerikorpi P., 2011, in Bastien P., Manset N., Clemens D. P., St-Louis N., eds, *Astronomical Society of the Pacific Conference Series Vol. 449, Astronomical Polarimetry 2008: Science from Small to Large Telescopes*. p. 157
 Berdyugin A., Piirola V., Teerikorpi P., 2014, *A&A*, **561**, A24
 Berkhuijsen E. M., Haslam C. G. T., Salter C. J., 1971, *A&A*, **14**, 252
 Blitz L., 1991, in Bloemen H., ed., *IAU Symposium Vol. 144, The Interstellar Disk-Halo Connection in Galaxies*. pp 41–52
 Bobylev V. V., Bajkova A. T., 2007, *Astronomy Letters*, **33**, 571
 Burkert A., Hartmann L., 2004, *ApJ*, **616**, 288
 Cernis K., Straizys V., 1992, *Baltic Astronomy*, **1**, 163
 Chandrasekhar S., Fermi E., 1953, *ApJ*, **118**, 113
 Clemens D. P., 2012, *ApJ*, **748**, 18
 Crutcher R. M., 2004, *Ap&SS*, **292**, 225
 Crutcher R., 2005, in Chyzy K. T., Otmianowska-Mazur K., Soida M., Dettmar R.-J., eds, *The Magnetized Plasma in Galaxy Evolution*. pp 103–110
 Crutcher R. M., Nutter D. J., Ward-Thompson D., Kirk J. M., 2004, *ApJ*, **600**, 279
 Cutri R. M., et al., 2003, *VizieR Online Data Catalog*, **2246**
 Desert F. X., Bazell D., Boulanger F., 1988, *ApJ*, **334**, 815
 Dickens J. E., Irvine W. M., Snell R. L., Bergin E. A., Schloerb F. P., Pratap P., Miralles M. P., 2000, *ApJ*, **542**, 870
 Dobashi K., 2011, *PASJ*, **63**, S1
 Dutra C. M., Bica E., 2002, *A&A*, **383**, 631
 Ellis R. S., Axon D. J., 1978, *Ap&SS*, **54**, 425
 Eswaraiah C., Pandey A. K., Maheswar G., Medhi B. J., Pandey J. C., Ojha D. K., Chen W. P., 2011, *MNRAS*, **411**, 1418

Eswaraiah C., Maheswar G., Pandey A. K., Jose J., Ramaprakash A. N., Bhatt H. C., 2013, *A&A*, **556**, A65
 Fejes I., Wesselius P. R., 1973, *A&A*, **24**, 1
 Franco G. A. P., 1989, *aap*, **223**, 313
 Franco G. A. P., Alves F. O., Girart J. M., 2010, *ApJ*, **723**, 146
 Gaia Collaboration 2016, *VizieR Online Data Catalog*, **1337**
 Gazol-Patiño A., Passot T., 1999, *ApJ*, **518**, 748
 Goldsmith P. F., Heyer M., Narayanan G., Snell R., Li D., Brunt C., 2008, *ApJ*, **680**, 428
 Green G. M., et al., 2014, *ApJ*, **783**, 114
 Hartmann D., Magnani L., Thaddeus P., 1998, *ApJ*, **492**, 205
 Heiles C., 2000, *AJ*, **119**, 923
 Heitsch F., Burkert A., Hartmann L. W., Slyz A. D., Devriendt J. E. G., 2005, *ApJ*, **633**, L113
 Heitsch F., Hartmann L. W., Slyz A. D., Devriendt J. E. G., Burkert A., 2008a, *ApJ*, **674**, 316
 Heitsch F., Hartmann L. W., Burkert A., 2008b, *ApJ*, **683**, 786
 Heitsch F., Stone J. M., Hartmann L. W., 2009, *ApJ*, **695**, 248
 Hennebelle P., 2013, in Kawabe R., Kuno N., Yamamoto S., eds, *Astronomical Society of the Pacific Conference Series Vol. 476, New Trends in Radio Astronomy in the ALMA Era: The 30th Anniversary of Nobeyama Radio Observatory*. p. 115
 Hennebelle P., Audit E., 2007, *A&A*, **465**, 431
 Hennebelle P., Pérault M., 1999, *A&A*, **351**, 309
 Hennebelle P., Pérault M., 2000, *A&A*, **359**, 1124
 Heyer M., Goldsmith P. F., Yıldız U. A., Snell R. L., Falgarone E., Pineda J. L., 2016, *MNRAS*, **461**, 3918
 Inoue T., Inutsuka S.-i., 2008, *ApJ*, **687**, 303
 Inoue T., Inutsuka S.-i., 2009, *ApJ*, **704**, 161
 Inoue T., Inutsuka S.-i., 2012, *ApJ*, **759**, 35
 Inoue T., Inutsuka S.-i., 2016, *ApJ*, **833**, 10

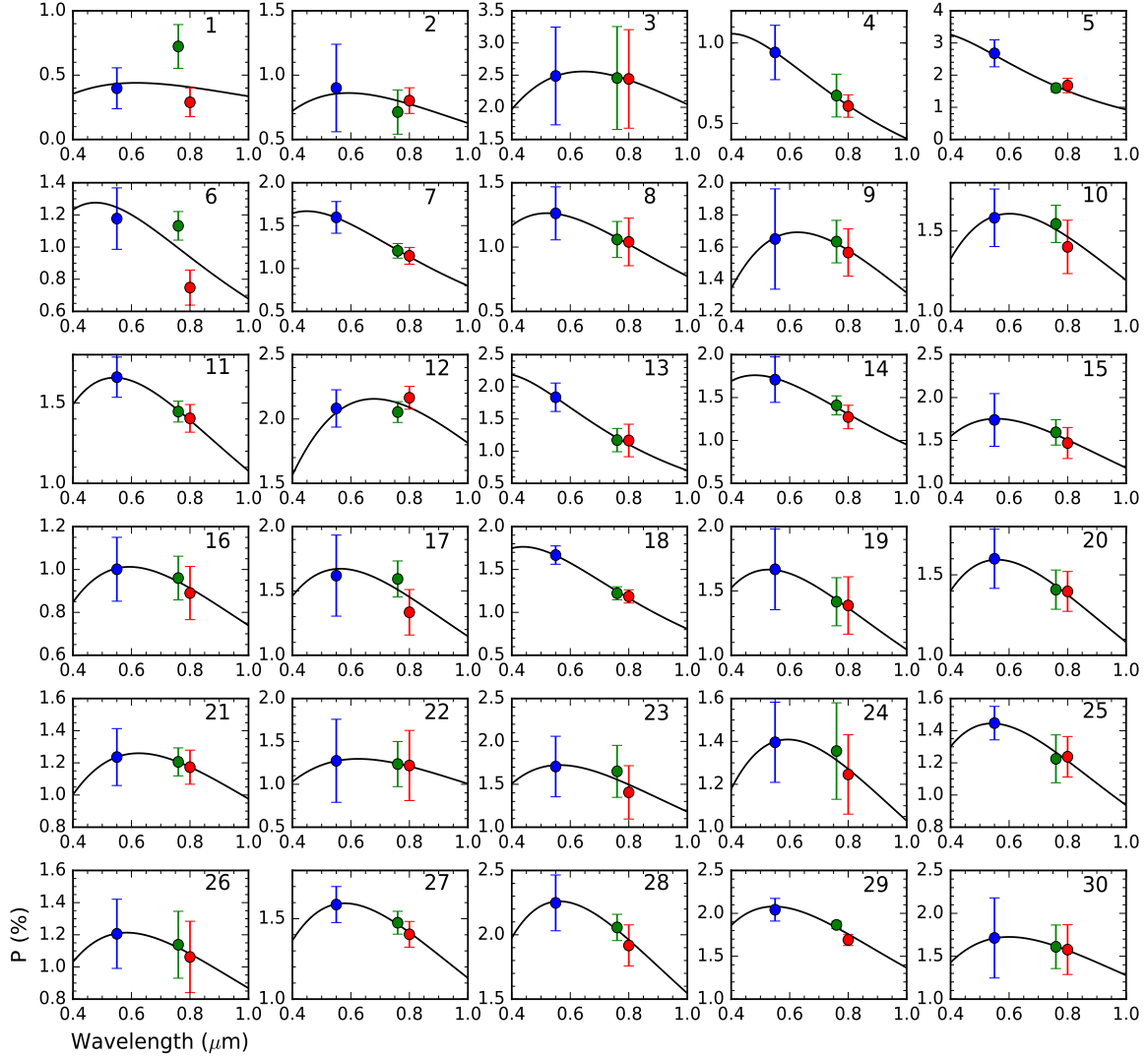


Figure 9. Interstellar linear polarization curves for 30 stars with the wavelength fitted using Serkowski's law (Serkowski et al., 1975). Blue, green and red circles are observed polarization values for V, R and I filters, respectively. Fitting to each group of VRI points has been shown. The star IDs corresponding to table 6 has been shown in each panel.

Inoue T., Inutsuka S.-i., Koyama H., 2007, *ApJ*, 658, L99

Inutsuka S.-I., Koyama H., 2002, *Ap&SS*, 281, 67

Inutsuka S.-I., Koyama H., Inoue T., 2005, in de Gouveia dal Pino E. M., Lugones G., Lazarian A., eds, American Institute of Physics Conference Series Vol. 784, Magnetic Fields in the Universe: From Laboratory and Stars to Primordial Structures.. pp 318–328, doi:10.1063/1.2077195

Juvela M., Mattila K., Lehtinen K., Lemke D., Laureijs R., Prusti T., 2002, *A&A*, 382, 583

Kauffmann J., Bertoldi F., Bourke T. L., Evans II N. J., Lee C. W., 2008, *A&A*, 487, 993

Keto E. R., Myers P. C., 1986, *ApJ*, 304, 466

Kirk J. M., Ward-Thompson D., André P., 2005, *MNRAS*, 360, 1506

Kirk J. M., Crutcher R. M., Ward-Thompson D., 2009, *ApJ*, 701, 1044

Korhonen T., Reiz A., 1986, *A&AS*, 64, 487

Koyama H., Inutsuka S.-I., 2000, *ApJ*, 532, 980

Lai S.-P., Crutcher R. M., Girart J. M., Rao R., 2001, *ApJ*, 561, 864

Lallement R., Welsh B. Y., Vergely J. L., Crifo F., Sfeir D., 2003, *A&A*, 411, 447

Large M. I., Quigley M. F. S., Haslam C. G. T., 1966, *MNRAS*, 131, 335

Laureijs R. J., Fukui Y., Helou G., Mizuno A., Imaoka K., Clark F. O., 1995, *ApJS*, 101, 87

Lee C. W., Myers P. C., 2011, *ApJ*, 734, 60

Lee C. W., Myers P. C., Tafalla M., 2001, *ApJS*, 136, 703

Lehtinen K., Mattila K., Lemke D., Juvela M., Prusti T., Laureijs R., 2003, *A&A*, 398, 571

Luhman K. L., 2001, *ApJ*, 560, 287

Lynds B. T., 1962, *ApJS*, 7, 1

Magnani L., Blitz L., Mundy L., 1985, *ApJ*, 295, 402

Magnani L., Hartmann D., Speck B. G., 1996, *ApJS*, 106, 447

Maheswar G., Lee C. W., Bhatt H. C., Mallik S. V., Dib S., 2010, *A&A*, 509, A44

Maheswar G., Lee C. W., Dib S., 2011, *A&A*, 536, A99

Maíz-Apellániz J., Walborn N. R., Galué H. Á., Wei L. H., 2004, *ApJS*, 151, 103

Malinen J., et al., 2014, *A&A*, 563, A125

Markkanen T., 1979, *A&A*, 74, 201

Mathewson D. S., Ford V. L., 1970, *Mem. RAS*, 74, 139

McCray R., Kafatos M., 1987, *ApJ*, 317, 190

McGehee P. M., 2008, *Star Formation and Molecular Clouds at High Galactic Latitude*. p 813

Medhi B. J., Maheswar G., Pandey J. C., Kumar T. S., Sagar R., 2008, *MNRAS*, 388, 105

- Neha S., Maheswar G., Soam A., Lee C. W., Tej A., 2016, *A&A*, **588**, A45
- Ntormousi E., Burkert A., Fierlinger K., Heitsch F., 2011, *ApJ*, **731**, 13
- Ostriker E. C., Stone J. M., Gammie C. F., 2001, *ApJ*, **546**, 980
- Pagani L., et al., 2003, *A&A*, **406**, L59
- Pagani L., Pardo J.-R., Apponi A. J., Bacmann A., Cabrit S., 2005, *A&A*, **429**, 181
- Pagani L., Bacmann A., Cabrit S., Vastel C., 2007, *A&A*, **467**, 179
- Palmeirim P., et al., 2013, *A&A*, **550**, A38
- Passot T., Vazquez-Semadeni E., Pouquet A., 1995, *ApJ*, **455**, 536
- Planck Collaboration et al., 2015, *A&A*, **576**, A104
- Planck Collaboration et al., 2016, *A&A*, **586**, A135
- Preibisch T., Zinnecker H., 1999, *AJ*, **117**, 2381
- Ramaprakash A. N., Gupta R., Sen A. K., Tandon S. N., 1998, *A&AS*, **128**, 369
- Rautela B. S., Joshi G. C., Pandey J. C., 2004, *Bulletin of the Astronomical Society of India*, **32**, 159
- Reach W. T., Wall W. F., Odegard N., 1998, *ApJ*, **507**, 507
- Rieke G. H., Lebofsky M. J., 1985, *ApJ*, **288**, 618
- Saury E., Miville-Deschênes M.-A., Hennebelle P., Audit E., Schmidt W., 2014, *A&A*, **567**, A16
- Schlafly E. F., et al., 2014, *ApJ*, **786**, 29
- Schmidt G. D., Elston R., Lupie O. L., 1992, *AJ*, **104**, 1563
- Serkowski K., Mathewson D. S., Ford V. L., 1975, *ApJ*, **196**, 261
- Sharpless S., 1959, *ApJS*, **4**, 257
- Shin M.-S., Stone J. M., Snyder G. F., 2008, *ApJ*, **680**, 336
- Skrutskie M. F., et al., 2006, *AJ*, **131**, 1163
- Soam A., Maheswar G., Bhatt H. C., Lee C. W., Ramaprakash A. N., 2013, *MNRAS*, **432**, 1502
- Soam A., Maheswar G., Lee C. W., Dib S., Bhatt H. C., Tamura M., Kim G., 2015, *A&A*, **573**, A34
- Toth L. V., Haikala L. K., Liljestroem T., Mattila K., 1995, *A&A*, **295**, 755
- Vazquez-Semadeni E., Passot T., Pouquet A., 1995, *ApJ*, **441**, 702
- Vázquez-Semadeni E., Ryu D., Passot T., González R. F., Gazol A., 2006, *ApJ*, **643**, 245
- Ward-Thompson D., André P., Kirk J. M., 2002, *MNRAS*, **329**, 257
- Whittet D. C. B., van Breda I. G., 1978, *A&A*, **66**, 57
- de Avillez M. A., 2000, *MNRAS*, **315**, 479
- de Avillez M. A., Breitschwerdt D., 2005, *A&A*, **436**, 585
- de Geus E. J., 1992, *A&A*, **262**, 258
- van Dishoeck E. F., Black J. H., 1988, *ApJ*, **334**, 771
- van Leeuwen F., 2007, *A&A*, **474**, 653

This paper has been typeset from a $\text{\TeX}/\text{\LaTeX}$ file prepared by the author.

Table 6: Polarization values of observed Tycho stars in VRI filters.

Star ID	α (J2000) ($^{\circ}$)	δ (J2000) ($^{\circ}$)	$P_V \pm \epsilon_{P_V}$ (%)	$\theta_V \pm \epsilon_{\theta_V}$ ($^{\circ}$)	$P_R \pm \epsilon_{P_R}$ (%)	$\theta_R \pm \epsilon_{\theta_R}$ ($^{\circ}$)	$P_I \pm \epsilon_{P_I}$ (%)	$\theta_I \pm \epsilon_{\theta_I}$ ($^{\circ}$)	$\lambda_{max} \pm \epsilon_{\lambda_{max}}$ (%)	$P_{max} \pm \epsilon_{P_{max}}$ (μm)	$R_V \pm \epsilon_{R_V}$
1	234.666229	-7.290575	0.4 \pm 0.2	51 \pm 9	0.7 \pm 0.2	78 \pm 6	0.3 \pm 0.1	71 \pm 8	0.62 \pm 0.67	0.44 \pm 0.24	3.45 \pm 3.75
2	234.689987	-7.249656	0.9 \pm 0.3	82 \pm 4	0.7 \pm 0.2	80 \pm 6	0.8 \pm 0.1	81 \pm 3	0.59 \pm 0.17	0.86 \pm 0.16	3.31 \pm 0.96
3	234.697296	-7.267688	2.5 \pm 0.8	60 \pm 8	2.5 \pm 0.8	65 \pm 8	2.4 \pm 0.8	70 \pm 9	0.64 \pm 0.01	2.56 \pm 0.02	3.61 \pm 0.20
4	234.747787	-7.236612	0.9 \pm 0.2	62 \pm 5	0.7 \pm 0.1	57 \pm 5	0.6 \pm 0.1	51 \pm 3	0.40 \pm 0.01	1.06 \pm 0.04	2.25 \pm 0.13
5	234.759399	-7.262989	2.7 \pm 0.4	23 \pm 4	1.6 \pm 0.1	28 \pm 2	1.7 \pm 0.2	31 \pm 4	0.35 \pm 0.07	3.33 \pm 1.15	1.95 \pm 0.40
MBM33											
6	237.439326	-5.811189	1.2 \pm 0.2	85 \pm 4	1.1 \pm 0.1	82 \pm 2	0.7 \pm 0.1	80 \pm 3	0.48 \pm 0.24	1.28 \pm 0.65	2.67 \pm 1.34
7	237.521911	-5.932307	1.6 \pm 0.2	79 \pm 3	1.2 \pm 0.1	80 \pm 2	1.1 \pm 0.1	84 \pm 2	0.45 \pm 0.01	1.67 \pm 0.04	2.52 \pm 0.15
8	237.569725	-5.859141	1.3 \pm 0.2	85 \pm 4	1.1 \pm 0.1	80 \pm 2	1.0 \pm 0.2	79 \pm 3	0.52 \pm 0.02	1.26 \pm 0.03	2.91 \pm 0.18
9	237.417944	-5.917022	1.6 \pm 0.3	81 \pm 5	1.6 \pm 0.1	79 \pm 2	1.6 \pm 0.1	80 \pm 2	0.63 \pm 0.03	1.69 \pm 0.03	3.51 \pm 0.22
10	237.405578	-5.779075	1.6 \pm 0.2	92 \pm 3	1.5 \pm 0.1	92 \pm 1	1.4 \pm 0.2	92 \pm 2	0.60 \pm 0.05	1.61 \pm 0.07	3.37 \pm 0.32
11	237.660440	-5.898259	1.7 \pm 0.1	87 \pm 2	1.4 \pm 0.1	86 \pm 1	1.4 \pm 0.1	86 \pm 1	0.54 \pm 0.01	1.66 \pm 0.02	3.04 \pm 0.17
12	237.287787	-5.928377	2.1 \pm 0.1	98 \pm 1	2.1 \pm 0.1	98 \pm 1	2.2 \pm 0.1	101 \pm 1	0.68 \pm 0.08	2.16 \pm 0.09	3.80 \pm 0.48
13	237.674831	-5.749450	1.8 \pm 0.2	86 \pm 3	1.2 \pm 0.2	81 \pm 4	1.2 \pm 0.3	80 \pm 5	0.37 \pm 0.03	2.21 \pm 0.21	2.06 \pm 0.18
14	237.256837	-5.757691	1.7 \pm 0.3	84 \pm 4	1.4 \pm 0.1	83 \pm 1	1.3 \pm 0.1	83 \pm 2	0.48 \pm 0.03	1.76 \pm 0.13	2.69 \pm 0.24
15	237.745219	-5.842658	1.7 \pm 0.3	87 \pm 4	1.6 \pm 0.1	84 \pm 2	1.5 \pm 0.2	85 \pm 3	0.56 \pm 0.04	1.75 \pm 0.08	3.11 \pm 0.26
16	237.676361	-6.036192	1.0 \pm 0.1	72 \pm 4	1.0 \pm 0.1	75 \pm 2	0.9 \pm 0.1	76 \pm 3	0.59 \pm 0.03	1.01 \pm 0.03	3.32 \pm 0.25
17	237.760799	-6.024821	1.6 \pm 0.3	76 \pm 5	1.6 \pm 0.1	79 \pm 2	1.3 \pm 0.2	85 \pm 3	0.56 \pm 0.13	1.67 \pm 0.26	3.16 \pm 0.75
18	237.620548	-6.144651	1.7 \pm 0.1	88 \pm 1	1.2 \pm 0.1	78 \pm 1	1.2 \pm 0.1	77 \pm 1	0.44 \pm 0.02	1.76 \pm 0.08	2.46 \pm 0.17
19	237.684774	-6.159001	1.7 \pm 0.3	86 \pm 5	1.4 \pm 0.2	82 \pm 3	1.4 \pm 0.2	81 \pm 4	0.53 \pm 0.02	1.67 \pm 0.04	2.96 \pm 0.19
20	237.894932	-5.935640	1.6 \pm 0.2	88 \pm 2	1.4 \pm 0.1	82 \pm 2	1.4 \pm 0.1	82 \pm 2	0.56 \pm 0.02	1.59 \pm 0.04	3.13 \pm 0.21
21	237.916806	-5.985692	1.2 \pm 0.2	84 \pm 3	1.2 \pm 0.1	81 \pm 1	1.2 \pm 0.1	82 \pm 2	0.62 \pm 0.00	1.26 \pm 0.00	3.50 \pm 0.19
22	237.858470	-6.120708	1.3 \pm 0.5	78 \pm 1	1.2 \pm 0.3	76 \pm 5	1.2 \pm 0.4	82 \pm 8	0.63 \pm 0.01	1.30 \pm 0.01	3.50 \pm 0.20
23	237.746356	-6.276022	1.7 \pm 0.4	76 \pm 5	1.7 \pm 0.3	82 \pm 5	1.4 \pm 0.3	83 \pm 6	0.56 \pm 0.08	1.72 \pm 0.14	3.15 \pm 0.45
24	237.738667	-6.328300	1.4 \pm 0.2	81 \pm 3	1.4 \pm 0.2	82 \pm 4	1.2 \pm 0.2	82 \pm 3	0.59 \pm 0.03	1.41 \pm 0.04	3.32 \pm 0.24
25	237.979203	-6.117325	1.4 \pm 0.1	81 \pm 1	1.2 \pm 0.1	77 \pm 3	1.2 \pm 0.1	81 \pm 2	0.54 \pm 0.02	1.45 \pm 0.04	3.03 \pm 0.21
26	237.764368	-6.413710	1.2 \pm 0.2	85 \pm 4	1.1 \pm 0.2	82 \pm 4	1.1 \pm 0.2	78 \pm 5	0.58 \pm 0.02	1.21 \pm 0.02	3.26 \pm 0.21
MBM35											
27	237.756650	-2.094230	1.6 \pm 0.1	80 \pm 2	1.5 \pm 0.1	85 \pm 1	1.4 \pm 0.1	90 \pm 2	0.58 \pm 0.01	1.60 \pm 0.02	3.24 \pm 0.19
28	237.790670	-2.142240	2.2 \pm 0.2	78 \pm 3	2.1 \pm 0.1	82 \pm 1	1.9 \pm 0.2	87 \pm 2	0.56 \pm 0.03	2.26 \pm 0.07	3.15 \pm 0.22
29	237.808010	-2.153560	2.0 \pm 0.1	78 \pm 2	1.9 \pm 0.0	79 \pm 1	1.7 \pm 0.1	85 \pm 1	0.55 \pm 0.06	2.08 \pm 0.17	3.06 \pm 0.37
30	237.830030	-2.148890	1.7 \pm 0.5	75 \pm 7	1.6 \pm 0.3	81 \pm 4	1.6 \pm 0.3	90 \pm 5	0.60 \pm 0.01	1.72 \pm 0.02	3.36 \pm 0.19

Table 7. Polarization results of 234 stars observed in the direction of MBM33-39 cloud complex with $P/\sigma_P \geq 2$.

Star ID	α (J2000) ($^{\circ}$)	δ (J2000) ($^{\circ}$)	l ($^{\circ}$)	b ($^{\circ}$)	$P \pm \epsilon_P$ (%)	$\theta \pm \epsilon_{\theta}$ ($^{\circ}$)	$\theta_{Galactic}$ ($^{\circ}$)
1	234.664825	-7.243520	358.732	36.915	1.2 ± 0.3	77 ± 7	125
2	234.666275	-7.290588	358.690	36.882	0.7 ± 0.2	78 ± 6	126
3	234.689941	-7.249604	358.747	36.892	0.7 ± 0.2	80 ± 6	128
4	234.692627	-7.273990	358.727	36.874	0.6 ± 0.1	72 ± 6	120
5	234.700455	-7.262742	358.744	36.875	1.5 ± 0.5	60 ± 8	108
6	234.707031	-7.170176	358.835	36.932	1.7 ± 0.2	66 ± 4	114
7	234.712326	-7.138198	358.870	36.950	0.6 ± 0.1	70 ± 3	118
8	234.716324	-7.120708	358.889	36.959	1.0 ± 0.3	67 ± 7	115
9	234.717743	-7.104168	358.906	36.969	0.7 ± 0.3	57 ± 9	105
10	234.732742	-7.230433	358.801	36.873	0.4 ± 0.1	71 ± 3	119
11	234.736481	-7.179309	358.851	36.905	0.6 ± 0.1	81 ± 3	129
12	234.739532	-7.227524	358.809	36.870	1.0 ± 0.5	48 ± 11	96
13	234.745026	-7.086656	358.945	36.960	0.8 ± 0.1	74 ± 5	122
14	234.747818	-7.236627	358.808	36.858	0.7 ± 0.1	57 ± 5	105
15	234.760971	-7.097479	358.948	36.941	0.9 ± 0.2	61 ± 7	109
16	234.824615	-7.261821	358.848	36.785	1.6 ± 0.4	44 ± 7	92
17	234.890594	-7.439786	358.738	36.617	0.9 ± 0.3	100 ± 8	148
18	234.896805	-7.027812	359.125	36.888	0.9 ± 0.1	63 ± 2	111
19	234.925552	-7.420925	358.784	36.604	0.5 ± 0.2	100 ± 11	148
20	234.930389	-7.418399	358.790	36.602	0.3 ± 0.1	75 ± 6	123
21	234.940918	-7.048465	359.142	36.841	1.9 ± 0.1	78 ± 1	126
22	234.947113	-6.995152	359.197	36.872	2.4 ± 0.6	65 ± 7	113
23	234.953140	-7.030041	359.170	36.844	2.3 ± 0.4	77 ± 5	125
24	234.954727	-7.400796	358.827	36.596	1.5 ± 0.2	89 ± 3	137
25	234.957733	-7.381444	358.847	36.606	1.3 ± 0.3	83 ± 7	131
26	234.959579	-7.380103	358.850	36.606	1.2 ± 0.1	73 ± 2	121
27	234.964523	-7.052097	359.159	36.821	2.6 ± 1.1	93 ± 12	141
28	235.066238	-6.975558	359.314	36.797	2.2 ± 0.6	96 ± 8	144
29	235.073257	-6.928510	359.363	36.823	1.1 ± 0.4	84 ± 9	132
30	235.091385	-6.909038	359.397	36.823	2.7 ± 0.5	80 ± 5	128
31	235.096268	-7.356310	358.985	36.521	1.5 ± 0.1	74 ± 2	122
32	235.102219	-7.320977	359.023	36.540	2.1 ± 0.6	90 ± 20	138
33	235.102951	-7.296313	359.046	36.556	1.0 ± 0.2	75 ± 5	123
34	235.104874	-7.352910	358.995	36.517	1.0 ± 0.5	82 ± 16	130
35	235.154037	-7.247395	359.133	36.551	1.6 ± 0.5	89 ± 9	137
36	235.163086	-7.247187	359.141	36.544	1.8 ± 0.1	91 ± 1	139
37	235.166168	-6.948177	359.422	36.741	1.6 ± 0.1	78 ± 1	126
38	235.167191	-6.953535	359.418	36.737	2.3 ± 0.7	89 ± 9	137
39	235.182129	-7.263934	359.141	36.519	1.4 ± 0.3	117 ± 6	165
40	235.185669	-7.191573	359.211	36.565	2.0 ± 0.1	100 ± 2	148
41	235.206650	-7.242327	359.181	36.515	2.2 ± 0.1	85 ± 1	133
42	235.243393	-6.988899	359.447	36.657	1.0 ± 0.1	96 ± 4	144
43	235.253021	-6.980438	359.463	36.655	1.4 ± 0.1	97 ± 2	145
44	235.306229	-7.133462	359.364	36.514	1.4 ± 0.5	89 ± 9	137
45	235.322968	-7.150585	359.362	36.490	1.2 ± 0.1	78 ± 2	126
46	235.329102	-7.145841	359.372	36.489	1.6 ± 0.5	69 ± 8	117
47	235.349609	-7.066414	359.462	36.526	1.3 ± 0.2	102 ± 4	150
48	235.367905	-7.076525	359.468	36.506	1.7 ± 0.3	66 ± 5	114
49	235.379730	-7.104511	359.451	36.479	0.8 ± 0.2	90 ± 6	138
50	237.253870	-1.864780	6.039	38.372	1.4 ± 0.1	92 ± 2	144
51	237.255371	-5.878733	2.108	35.864	1.6 ± 0.6	63 ± 10	113
52	237.255870	-1.874110	6.032	38.364	1.5 ± 0.3	87 ± 5	140
53	237.265854	-5.902115	2.094	35.842	1.5 ± 0.2	76 ± 5	126
54	237.275220	-1.878780	6.042	38.345	1.7 ± 0.1	82 ± 2	134
55	237.279709	-5.894644	2.112	35.836	2.4 ± 0.5	72 ± 6	122
56	237.280550	-1.853440	6.071	38.357	1.6 ± 0.3	87 ± 5	140
57	237.289220	-1.902780	6.029	38.320	1.2 ± 0.3	89 ± 6	142
58	237.298798	-5.929773	2.094	35.799	1.1 ± 0.1	87 ± 2	137
59	237.303900	-1.938780	6.004	38.286	1.1 ± 0.3	78 ± 8	131
60	237.308578	-5.884315	2.144	35.820	1.4 ± 0.3	79 ± 6	129

Table 7 – *continued*

Star ID	α (J2000) ($^{\circ}$)	δ (J2000) ($^{\circ}$)	l ($^{\circ}$)	b ($^{\circ}$)	$P \pm \epsilon_P$ (%)	$\theta \pm \epsilon_{\theta}$ ($^{\circ}$)	$\theta_{Galactic}$ ($^{\circ}$)
61	237.311900	-1.891440	6.058	38.309	1.5 ± 0.1	83 ± 1	136
62	237.320938	-5.921296	2.119	35.787	1.9 ± 0.3	87 ± 5	137
63	237.330383	-5.922173	2.126	35.779	1.4 ± 0.2	84 ± 4	134
64	237.335815	-5.898364	2.152	35.790	1.5 ± 0.3	93 ± 5	143
65	237.344498	-5.892202	2.165	35.788	1.3 ± 0.4	87 ± 9	137
66	237.351700	-5.949665	2.116	35.745	1.1 ± 0.1	78 ± 4	128
67	237.351868	-5.780048	2.277	35.854	1.0 ± 0.2	72 ± 5	122
68	237.352875	-5.859034	2.203	35.803	1.4 ± 0.1	76 ± 2	126
69	237.352890	-5.858979	2.203	35.803	1.2 ± 0.1	85 ± 2	135
70	237.353088	-5.775971	2.282	35.855	1.9 ± 0.3	87 ± 5	137
71	237.365494	-5.903028	2.171	35.765	2.0 ± 0.6	75 ± 8	125
72	237.374619	-5.854682	2.224	35.789	1.2 ± 0.5	90 ± 12	140
73	237.391388	-5.759244	2.328	35.837	1.9 ± 0.5	83 ± 8	133
74	237.404816	-6.003438	2.107	35.670	1.3 ± 0.2	81 ± 4	131
75	237.405304	-5.904298	2.201	35.733	1.8 ± 0.5	74 ± 7	124
76	237.408081	-5.839082	2.265	35.773	1.6 ± 0.2	82 ± 4	132
77	237.417755	-5.992552	2.127	35.667	1.7 ± 0.6	67 ± 9	117
78	237.424026	-5.955384	2.168	35.687	1.7 ± 0.3	89 ± 4	139
79	237.426605	-5.901800	2.220	35.719	1.8 ± 0.5	64 ± 8	114
80	237.437469	-5.903768	2.227	35.709	3.0 ± 0.6	83 ± 6	133
81	237.437714	-5.785320	2.340	35.785	2.2 ± 0.6	87 ± 8	137
82	237.448563	-5.951352	2.191	35.670	1.7 ± 0.2	88 ± 4	138
83	237.448563	-5.985734	2.158	35.648	1.8 ± 0.6	95 ± 9	145
84	237.452255	-6.092173	2.060	35.577	1.6 ± 0.1	84 ± 3	134
85	237.487640	-6.077678	2.102	35.560	1.7 ± 0.4	78 ± 7	128
86	237.493164	-6.100979	2.084	35.541	1.6 ± 0.6	74 ± 10	124
87	237.501923	-6.037074	2.151	35.575	1.5 ± 0.2	72 ± 4	122
88	237.537659	-5.914225	2.295	35.626	3.2 ± 0.9	73 ± 8	123
89	237.547300	-1.594130	6.541	38.302	0.8 ± 0.1	81 ± 2	134
90	237.556381	-5.910893	2.313	35.614	2.1 ± 0.6	90 ± 8	140
91	237.561127	-5.861592	2.364	35.641	1.3 ± 0.5	102 ± 10	152
92	237.573608	-5.892675	2.344	35.612	1.4 ± 0.4	103 ± 8	153
93	237.577881	-5.833573	2.403	35.646	1.4 ± 0.2	85 ± 5	135
94	237.585510	-5.881410	2.364	35.610	2.4 ± 0.6	88 ± 7	138
95	237.606903	-6.225999	2.055	35.374	1.9 ± 0.3	85 ± 4	135
96	237.608292	-5.869369	2.393	35.600	1.6 ± 0.2	85 ± 4	135
97	237.616135	-6.208387	2.079	35.378	1.8 ± 0.2	77 ± 3	127
98	237.642258	-6.230644	2.078	35.344	1.6 ± 0.4	78 ± 7	128
99	237.674896	-6.129722	2.199	35.383	1.7 ± 0.2	87 ± 4	137
100	237.682358	-5.980763	2.345	35.473	1.9 ± 0.3	81 ± 4	131
101	237.688000	-1.452510	6.793	38.275	1.5 ± 0.3	83 ± 5	136
102	237.704025	-5.950323	2.391	35.475	1.5 ± 0.3	74 ± 6	124
103	237.709381	-6.003910	2.344	35.437	1.7 ± 0.6	85 ± 10	135
104	237.711685	-6.041290	2.311	35.411	1.3 ± 0.1	81 ± 2	131
105	237.719116	-6.180243	2.185	35.317	1.4 ± 0.1	82 ± 3	132
106	237.720078	-5.966722	2.388	35.453	1.3 ± 0.3	85 ± 5	135
107	237.721649	-5.970223	2.386	35.449	1.2 ± 0.4	94 ± 9	144
108	237.724228	-6.130367	2.237	35.345	1.4 ± 0.4	91 ± 8	141
109	237.724548	-6.144137	2.224	35.336	0.7 ± 0.2	77 ± 8	127
110	237.728363	-5.992858	2.370	35.430	1.4 ± 0.2	81 ± 4	131
111	237.730743	-6.148084	2.225	35.329	1.8 ± 0.4	93 ± 6	143
112	237.734010	-1.375170	6.907	38.284	1.5 ± 0.3	81 ± 5	134
113	237.736496	-6.106158	2.269	35.351	1.7 ± 0.3	89 ± 3	139
114	237.736680	-1.432510	6.851	38.248	1.5 ± 0.7	90 ± 13	143
115	237.737350	-1.415840	6.868	38.257	1.3 ± 0.3	80 ± 6	133
116	237.739227	-6.099532	2.277	35.353	1.6 ± 0.6	67 ± 10	117
117	237.741058	-6.186683	2.196	35.296	1.7 ± 0.4	82 ± 7	132
118	237.756650	-2.094230	6.196	37.833	1.5 ± 0.1	85 ± 1	138
119	237.760818	-6.024866	2.365	35.384	1.5 ± 0.3	85 ± 4	135
120	237.768234	-6.146307	2.256	35.301	1.9 ± 0.8	107 ± 12	157

Table 7 – continued

Star ID	α (J2000) ($^{\circ}$)	δ (J2000) ($^{\circ}$)	l ($^{\circ}$)	b ($^{\circ}$)	$P \pm \epsilon_P$ (%)	$\theta \pm \epsilon_{\theta}$ ($^{\circ}$)	$\theta_{Galactic}$ ($^{\circ}$)
121	237.785873	-6.090573	2.322	35.323	1.7 ± 0.5	77 ± 6	127
122	237.790670	-2.142240	6.174	37.776	2.1 ± 0.1	82 ± 1	135
123	237.808010	-2.153560	6.176	37.756	1.9 ± 0.1	79 ± 1	132
124	237.830030	-2.148890	6.197	37.741	1.6 ± 0.3	81 ± 4	134
125	237.850950	-1.513970	6.855	38.107	1.4 ± 0.4	79 ± 8	132
126	237.861950	-1.347710	7.031	38.199	1.0 ± 0.2	71 ± 4	125
127	237.865620	-1.513300	6.867	38.096	1.5 ± 0.1	84 ± 2	137
128	237.886960	-1.545300	6.850	38.060	1.6 ± 0.3	82 ± 5	136
129	237.895290	-1.364380	7.041	38.162	1.2 ± 0.2	82 ± 5	136
130	237.960640	-1.363040	7.092	38.110	2.1 ± 0.1	106 ± 1	160
131	238.023588	-4.332006	4.189	36.248	5.3 ± 2.6	66 ± 14	118
132	238.050981	-4.372278	4.171	36.201	3.6 ± 1.2	69 ± 9	120
133	238.071911	-4.324807	4.233	36.214	2.4 ± 0.1	74 ± 1	126
134	238.082026	-4.336071	4.230	36.200	5.1 ± 2.1	73 ± 11	124
135	238.167678	-4.207979	4.420	36.212	1.6 ± 0.1	65 ± 2	116
136	238.173347	-4.248406	4.385	36.183	2.1 ± 0.1	72 ± 1	124
137	238.189188	-4.824758	3.840	35.811	1.9 ± 0.1	64 ± 1	115
138	238.196004	-4.175669	4.473	36.210	1.9 ± 0.4	78 ± 6	130
139	238.209161	-4.165420	4.494	36.206	2.1 ± 0.1	76 ± 1	128
140	238.224603	-4.210609	4.461	36.166	1.9 ± 0.3	75 ± 5	127
141	238.229792	-4.870920	3.827	35.751	1.7 ± 0.1	69 ± 1	120
142	238.233564	-4.158268	4.519	36.191	2.3 ± 0.2	74 ± 2	125
143	238.267636	-4.250212	4.456	36.108	1.2 ± 0.4	65 ± 8	116
144	238.275569	-4.203571	4.507	36.131	1.8 ± 0.1	81 ± 2	133
145	238.314770	-3.194860	5.525	36.721	2.0 ± 0.1	83 ± 1	135
146	238.341834	-4.378782	4.388	35.970	2.6 ± 0.1	76 ± 1	127
147	238.355248	-4.347309	4.429	35.979	2.7 ± 0.1	78 ± 1	130
148	238.365447	-4.299565	4.483	36.001	2.5 ± 0.2	77 ± 2	129
149	238.449810	-3.034300	5.787	36.712	3.1 ± 0.1	84 ± 1	137
150	238.493830	-3.042060	5.812	36.672	2.5 ± 0.1	102 ± 1	155
151	238.576830	-3.202710	5.717	36.509	3.6 ± 0.2	94 ± 2	146
152	238.581580	-3.129170	5.793	36.550	1.8 ± 0.1	95 ± 2	148
153	238.608153	-4.895051	4.093	35.441	2.5 ± 0.1	97 ± 2	148
154	238.625497	-4.900464	4.101	35.424	1.7 ± 0.1	89 ± 2	140
155	238.667280	-3.364380	5.626	36.339	3.1 ± 0.1	96 ± 1	148
156	238.714760	-3.395930	5.631	36.282	3.4 ± 0.1	105 ± 1	157
157	238.746060	-3.520360	5.532	36.181	2.3 ± 0.1	94 ± 1	146
158	238.747170	-3.400650	5.651	36.253	2.8 ± 0.1	100 ± 1	152
159	238.752880	-4.419318	4.662	35.623	1.8 ± 0.2	89 ± 3	141
160	238.756890	-3.389780	5.668	36.252	2.2 ± 0.1	87 ± 1	139
161	238.785680	-3.513780	5.568	36.154	2.7 ± 0.1	94 ± 2	146
162	238.795840	-3.177160	5.907	36.351	2.7 ± 0.1	89 ± 1	142
163	238.804692	-4.371314	4.747	35.612	1.9 ± 0.3	85 ± 5	137
164	238.808233	-4.401561	4.721	35.591	1.9 ± 0.2	88 ± 2	140
165	238.813560	-3.165470	5.932	36.344	2.5 ± 0.1	105 ± 1	158
166	238.871850	-3.287220	5.857	36.223	2.2 ± 0.1	88 ± 1	141
167	238.893670	-3.314560	5.846	36.190	2.2 ± 0.1	86 ± 1	139
168	238.900830	-3.313320	5.853	36.185	2.1 ± 0.1	85 ± 1	138
169	238.908540	-3.146380	6.022	36.280	4.6 ± 0.3	112 ± 2	165
170	238.923610	-3.184580	5.996	36.245	3.2 ± 0.1	105 ± 1	158
171	238.938600	-3.169830	6.022	36.242	2.8 ± 0.2	101 ± 2	154
172	239.044520	-3.325680	5.948	36.063	2.4 ± 0.1	92 ± 1	145
173	239.047040	-3.327360	5.948	36.060	2.6 ± 0.1	90 ± 1	143
174	239.155790	-3.388940	5.969	35.937	2.6 ± 0.1	98 ± 1	151
175	239.489430	-3.547650	6.063	35.576	2.0 ± 0.2	88 ± 3	141
176	239.518830	-3.587160	6.046	35.528	2.1 ± 0.2	84 ± 3	137
177	239.521390	-3.574160	6.061	35.534	2.0 ± 0.1	92 ± 2	145
178	239.521460	-3.542270	6.092	35.553	2.0 ± 0.1	86 ± 2	139
179	239.799280	-1.526560	8.298	36.533	1.2 ± 0.3	80 ± 6	134
180	239.803790	-1.930900	7.894	36.291	1.6 ± 0.2	89 ± 3	143

Table 7 – *continued*

Star ID	α (J2000) ($^{\circ}$)	δ (J2000) ($^{\circ}$)	l ($^{\circ}$)	b ($^{\circ}$)	$P \pm \epsilon_P$ (%)	$\theta \pm \epsilon_{\theta}$ ($^{\circ}$)	$\theta_{Galactic}$ ($^{\circ}$)
181	239.805130	-1.875570	7.951	36.323	1.3 ± 0.3	103 ± 6	157
182	239.821140	-1.919570	7.919	36.284	1.3 ± 0.1	87 ± 2	140
183	239.833960	-1.483890	8.366	36.530	0.6 ± 0.3	88 ± 10	142
184	239.851300	-1.504560	8.357	36.504	0.5 ± 0.1	88 ± 6	142
185	239.855970	-1.506560	8.358	36.499	0.7 ± 0.1	86 ± 4	140
186	239.862640	-1.432560	8.438	36.538	0.5 ± 0.2	65 ± 9	119
187	239.864640	-1.466560	8.405	36.515	0.6 ± 0.3	60 ± 11	114
188	239.899280	-1.749280	8.146	36.322	1.9 ± 0.5	89 ± 8	143
189	239.906260	-1.302680	8.601	36.578	0.8 ± 0.1	77 ± 3	132
190	239.918250	-1.800980	8.108	36.276	1.7 ± 0.1	95 ± 1	149
191	239.953610	-1.328680	8.609	36.525	0.9 ± 0.2	76 ± 5	130
192	239.966280	-1.316080	8.636	36.525	1.0 ± 0.2	75 ± 5	130
193	239.974950	-1.316070	8.635	36.519	1.8 ± 0.4	81 ± 6	135
194	239.983780	-1.743370	8.214	36.256	2.1 ± 0.1	97 ± 1	151
195	240.067820	-1.710040	8.309	36.209	1.7 ± 0.2	105 ± 3	159
196	240.095830	-1.388480	8.652	36.374	1.0 ± 0.1	83 ± 3	137
197	240.126800	-1.412810	8.650	36.335	0.8 ± 0.4	97 ± 12	151
198	240.140400	-1.374960	8.698	36.346	1.4 ± 0.6	94 ± 12	149
199	240.150360	-1.415330	8.665	36.314	1.2 ± 0.1	105 ± 3	159
200	240.160870	-1.407540	8.680	36.310	0.5 ± 0.2	80 ± 9	134
201	240.216730	-1.160040	8.970	36.409	1.0 ± 0.2	104 ± 5	159
202	240.276740	-1.219370	8.954	36.326	1.0 ± 0.1	90 ± 3	145
203	240.299410	-1.210700	8.979	36.312	0.6 ± 0.2	90 ± 9	144
204	240.306750	-1.562050	8.630	36.101	1.0 ± 0.1	84 ± 3	139
205	240.361430	-1.589380	8.642	36.041	1.0 ± 0.1	89 ± 3	143
206	240.370770	-1.520710	8.718	36.074	1.3 ± 0.6	100 ± 12	155
207	240.542190	-1.564570	8.797	35.909	0.8 ± 0.1	86 ± 3	141
208	240.544860	-1.605910	8.757	35.883	1.4 ± 0.4	78 ± 7	132
209	240.547530	-1.485240	8.881	35.950	1.4 ± 0.1	75 ± 2	130
210	240.580210	-1.563240	8.826	35.878	1.3 ± 0.3	77 ± 6	131
211	240.581540	-1.608570	8.781	35.851	0.8 ± 0.2	87 ± 6	141
212	240.986681	0.436293	11.148	36.691	0.4 ± 0.2	91 ± 12	147
213	241.059251	0.027519	10.779	36.401	0.8 ± 0.2	88 ± 7	144
214	241.070099	0.439281	11.210	36.624	1.0 ± 0.4	70 ± 9	126
215	241.071945	0.418463	11.190	36.611	0.7 ± 0.1	71 ± 4	127
216	241.134037	-0.022007	10.781	36.311	0.3 ± 0.1	107 ± 7	163
217	241.154955	0.004965	10.823	36.309	0.4 ± 0.2	99 ± 8	155
218	241.159661	0.053231	10.876	36.332	0.7 ± 0.1	67 ± 5	123
219	241.167785	0.699604	11.547	36.689	0.9 ± 0.1	74 ± 4	130
220	241.181238	0.731057	11.589	36.696	0.8 ± 0.2	67 ± 6	123
221	241.214128	0.740654	11.622	36.674	1.0 ± 0.1	64 ± 2	120
222	241.312445	-0.104714	10.822	36.117	0.5 ± 0.1	96 ± 6	151
223	241.448553	0.805944	11.852	36.516	1.4 ± 0.3	75 ± 6	131
224	241.451074	0.571298	11.612	36.383	1.7 ± 0.8	64 ± 12	120
225	241.465961	0.588172	11.639	36.380	0.8 ± 0.1	60 ± 4	116
226	241.488214	0.590887	11.658	36.363	1.2 ± 0.6	72 ± 13	128
227	241.504434	0.825280	11.911	36.480	2.1 ± 0.1	86 ± 1	142
228	241.524608	0.780546	11.878	36.438	0.9 ± 0.4	78 ± 11	134
229	241.683613	0.521306	11.721	36.162	0.3 ± 0.1	87 ± 9	143
230	241.722132	0.102803	11.319	35.896	0.6 ± 0.2	76 ± 7	132
231	241.732762	0.013001	11.235	35.836	0.6 ± 0.1	75 ± 3	131
232	241.754781	0.320812	11.565	35.991	0.9 ± 0.1	62 ± 4	118
233	241.756613	0.104295	11.345	35.868	1.5 ± 0.3	85 ± 5	141
234	241.767043	0.093198	11.341	35.853	0.5 ± 0.1	81 ± 3	137

Note: Column 1 shows the star id; column 2 represents right ascension (α) in increasing order; column 3 denotes the declination (δ); columns 4 & 5 show the Galactic longitude and latitude, respectively; column 6 represents the values of degree of polarization with errors; column 7 represents the polarization position angles with errors measured from the North increasing towards the East, and column 8 denotes the Galactic polarization position angles measured from the Galactic North.